Published in final edited form as:

Nature. 2024 August ; 632(8025): 656–663. doi:10.1038/s41586-024-07718-0.

SMYD5 methylation of rpL40 links ribosomal output to gastric cancer

Juhyung Park[1,10], **Jibo Wu**[2,10], **Krzysztof J. Szkop**[3], **Jinho Jeong**[1], **Predrag Jovanovic**[4], **Dylan Husmann**[1], **Natasha M. Flores**[2], **Joel W. Francis**[1], **Ying-Jiun C. Chen**[1,9], **Ana Morales Benitez**[2], **Emily Zahn**[5], **Shumei Song**[6], **Jaffer A. Ajani**[6], **Linghua Wang**[7], **Kamini Singh**[8], **Ola Larsson**[3], **Benjamin A. Garcia**[5], **Ivan Topisirovic**[4], **Or Gozani**[1,✉], **Pawel K. Mazur**[2,✉]

[1]Department of Biology, Stanford University, Stanford, CA, USA

[2]Department of Experimental Radiation Oncology, The University of Texas MD Anderson Cancer Center, Houston, TX, USA

[3]Department of Oncology-Pathology, Science for Life Laboratories, Karolinska Institute, Stockholm, Sweden

[4]Lady Davis Institute and Gerald Bronfman Department of Oncology, McGill University, Montreal, Quebec, Canada

[5]Department of Biochemistry and Molecular Biophysics, Washington University School of Medicine, St Louis, MO, USA

[6]Department of Gastrointestinal Medical Oncology, The University of Texas MD Anderson Cancer Center, Houston, TX, USA

[7]Department of Genomic Medicine, The University of Texas MD Anderson Cancer Center, Houston, TX, USA

[8]Department of Molecular Pharmacology, Albert Einstein College of Medicine, Montefiore Einstein Cancer Center, Bronx, NY, USA

✉ **Correspondence and requests for materials** should be addressed to Or Gozani, ogozani@stanford.edu; Pawel K. Mazur, pkmazur@mdanderson.org.

Author contributions J.P. and J.W. contributed equally to this work. They were responsible for the experimental design, execution, data analyses and manuscript preparation. K.J.S. performed polysomal RNA sequencing bioinformatics and GSEA analyses with advice from O.L. and I.T. J.J. with J.P. performed rpL40K22me3 antibody characterization and in vitro methylation assays. P.J., with help from J.P., performed northern blotting. J.W.F. generated ribosome PDB figures and D.H. performed AlphaFold modelling work. Y.-J.C.C. performed biochemical fractionation. J.P. and E.Z. performed MS experiments and analyses, with supervision from B.A.G. N.M.F. performed mouse model and IHC analyses. A.M.B. helped with animal studies. J.A.A. and S.S. provided PDX and clinical samples. L.W. helped with expression analyses and data interpretation. K.S., O.L. and I.T. advised on experimental design and data interpretation. O.G. and P.K.M. were equally responsible for supervision of research, data interpretation and manuscript preparation.

Competing interests O.G. is a co-scientific founder and stockholder of EpiCypher, K36 Therapeutics and Alternative Bio. P.K.M. is a consultant and stockholder of Ikena Oncology and Alternative bio. The other authors declare no competing interests.

Additional information

Supplementary information The online version contains supplementary material available at https://doi.org/10.1038/s41586-024-07718-0.

Peer review information *Nature* thanks Ernesto Guccione, Davide Ruggero, Toshikazu Ushijima and the other, anonymous, reviewer(s) for their contribution to the peer review of this work.

[9]Present address: Department of Epigenetics and Molecular Carcinogenesis, The University of Texas MD Anderson Cancer Center, Houston, TX, USA

[10]These authors contributed equally: Juhyung Park, Jibo Wu

Abstract

Dysregulated transcription due to disruption in histone lysine methylation dynamics is an established contributor to tumorigenesis[1,2]. However, whether analogous pathologic epigenetic mechanisms act directly on the ribosome to advance oncogenesis is unclear. Here we find that trimethylation of the core ribosomal protein L40 (rpL40) at lysine 22 (rpL40K22me3) by the lysine methyltransferase SMYD5 regulates mRNA translation output to promote malignant progression of gastric adenocarcinoma (GAC) with lethal peritoneal ascites. A biochemical-proteomics strategy identifies the monoubiquitin fusion protein partner rpL40 (ref. 3) as the principal physiological substrate of SMYD5 across diverse samples. Inhibiting the SMYD5-rpL40K22me3 axis in GAC cell lines reprogrammes protein synthesis to attenuate oncogenic gene expression signatures. SMYD5 and rpL40K22me3 are upregulated in samples from patients with GAC and negatively correlate with clinical outcomes. *SMYD5* ablation in vivo in familial and sporadic mouse models of malignant GAC blocks metastatic disease, including peritoneal carcinomatosis. Suppressing SMYD5 methylation of rpL40 inhibits human cancer cell and patient-derived GAC xenograft growth and renders them hypersensitive to inhibitors of PI3K and mTOR. Finally, combining SMYD5 depletion with PI3K-mTOR inhibition and chimeric antigen receptor T cell administration cures an otherwise lethal in vivo mouse model of aggressive GAC-derived peritoneal carcinomatosis. Together, our work uncovers a ribosome-based epigenetic mechanism that facilitates the evolution of malignant GAC and proposes SMYD5 targeting as part of a potential combination therapy to treat this cancer.

Gastric cancer is the third leading cause of cancer-related mortality in the world[4]. Surgical treatment is an option when GAC is detected before tumour dissemination[5]. Unfortunately, in countries that do not actively screen for gastric cancer, most patients at the time of diagnosis have developed metastatic disease and have limited therapeutic options, with spread to the peritoneum linked to incurable end-stage disease[5,6]. Thus, there is a critical need to identify clinically actionable pathways that regulate GAC progression. Dysregulation of lysine methylation is implicated in the pathogenesis of diverse cancers, and a growing number of lysine methyltransferase (KMT) inhibitors are being tested in clinical trials, with one already approved by the US Food and Drug Administration for oncological indications[7]. We therefore searched for KMTs with potential aetiological roles in GAC and identified SET and MYND domain-containing protein 5 (SMYD5) as a compelling candidate. Specifically, *SMYD5* expression was frequently upregulated in patients with GAC[8] (Fig. 1a) and showed a significant and strong negative correlation with patient survival and disease-free progression (Fig. 1b and Extended Data Fig. 1a). Moreover, *Smyd5* knockout mice were born at normal Mendelian ratios, viable into adulthood, fertile and essentially normal with only minor phenotypes (Extended Data Fig. 1b). These results suggest that potential therapeutic inhibition of SMYD5 would have minimal on-target toxicity.

SMYD5 harbours a catalytic lysine methyltransferase SET domain, and like other SMYD family members, the secondary sequence of this motif is discontinuous owing to an insertion of the MYND domain. Instead, the two separated SET regions are modelled to form an intact catalytic domain in three dimensions[9] (Extended Data Fig. 1c). Enzymatically, SMYD5 is reported to trimethylate histone H3 at K36 (H3K36me3) and histone H4 at K20 (H4K20me3)[10,11] in the context of histone octamers, but not on nucleosome substrates[10]. However, this purported histone methylation activity occurs independent of a functional SET domain[10], which suggests that the assignment of SMYD5 as a histone methyltransferase, like the case for some other KMTs, may be unreliable[12]. Accordingly, *SMYD5* knockdown in three different cell lines did not alter H3K36me3 or H4K20me3 levels (Extended Data Fig. 1d). Furthermore, we did not observe SMYD5 methylation activity in vitro on histone H3, histone H4, octamer or nucleosome substrates. This was in contrast to the positive control enzymes SETD2 and SUV420H1, which methylate H3K36 and H4K20, respectively (Extended Data Fig. 1e). Based on these results and the observation that SMYD5 localizes to the cytoplasm (Extended Data Fig. 1f), we speculated that a bona fide catalytic activity for SMYD5 is yet to be established.

SMYD5 generates endogenous rpL40K22me3

To identify a candidate physiological substrate (or substrates) of SMYD5, a CRISPR-guided biochemical-proteomics-coupled approach was taken. We generated a putative SMYD5 catalytic mutant (SMYD5(Y351A)) based on homology to SMYD2 and SMYD3 (Extended Data Fig. 1c) and used either recombinant wild-type or mutant SMYD5 to perform in vitro methylation assays with ^{3}H-labelled *S*-adenosyl-methionine (^{3}H-SAM) as the methyl donor on extracts from control or SMYD5-depleted cells as substrate (Fig. 1c). A single prominent band near 10 kDa was detected only in the reaction using wild-type recombinant SMYD5 enzyme and extract from *SMYD5* knockdown cells as the substrate (Fig. 1d). Notably, under similar conditions, a single approximately 10 kDa signal was the only band observed in two additional independent cell lines, and this band migrated lower than histone H4 (Extended Data Fig. 2a–c). These data argue that the approximately 10 kDa protein is methylated at nearly saturating stoichiometry, is unlikely to be a histone, and is the principal substrate of SMYD5 in multiple cell lines.

To identify the SMYD5 methylated band, the 10 kDa gel region from in vitro methylated *SMYD5* knockdown extracts was analysed by tandem mass spectrometry (MS/MS). Deuterated SAM was used as the methyl donor to distinguish SMYD5-catalysed methylation from all other sources[13]. However, no deuterated methyl peptides were identified (data not shown). We reasoned that this was because the methylated protein was low in abundance and/or the specific peptide was unconducive to MS/MS analysis. To address these issues, a five-step fractionation protocol was used to enrich the SMYD5-dependent methylated band for further MS/MS analyses (Fig. 1e, schematic). Despite significant enrichment of activity through fractionation (Extended Data Fig. 2d,e) and the use of six different proteases to optimize the probability of obtaining suitable peptides, we did not detect a deuterated methylated peptide by MS/MS. Nonetheless, when comparing the proteins present in the MS/MS datasets from the various fractions independent of methylation, one candidate—UBA52, which is reported as an interactor of SMYD5 in bioGRID[14]—was present as a strong hit in all fractions and was the top hit in the purest sample obtained after two-dimensional (2D) gel electrophoresis separation (Fig. 1e and Supplementary Tables 1–4). The *UBA52* gene encodes an amino-terminal ubiquitin fused to rpL40 at the carboxy terminus that is cleaved into free ubiquitin and rpL40, a 52-amino-acid protein component of the ribosomal 60S large subunit[3] (Fig. 1f). Notably, over 25 years ago, Edman degradation sequencing of rpL40 identified trimethylation of K22 at nearly 100% stoichiometry[15]. Note that the sequence surrounding K22 makes detection of K22me3-containing peptides by MS/MS challenging (Extended Data Fig. 3a). These observations led us to postulate that rpL40 is the 10 kDa substrate methylated by SMYD5 in extracts. Indeed, recombinant wild-type SMYD5, but not SMYD5(Y351A), methylated recombinant rpL40 in vitro (Fig. 1g), and substitution of K22 to an arginine (rpL40(K22R)) abolished this activity (Fig. 1h). SMYD5 also methylated uncleaved recombinant UBA52 in vitro, but did not methylate ubiquitin alone or several other proteins identified in the fractionation experiments or other putative SMYD5 substrates (Extended Data Fig. 3b–e and data not shown). Finally, direct in vitro side-by-side comparisons of rpL40 and histones showed that SMYD5 methylated rpL40, but did not show detectable activity on histone octamers or nucleosomes (Fig. 1i). We note that recombinant rpL40 migrates at 10 kDa despite consisting of only 52 amino acids (Fig. 1i). Together, our data demonstrate that SMYD5 specifically methylates rpL40 at K22 in vitro.

We next generated a state-specific rpL40K22me3 antibody, which selectively recognized rpL40 peptides in a K22me3-dependent manner, did not bind to 15 different peptides from other proteins harbouring a trimethyl lysine and recognized SMYD5-catalysed in vitro methylated rpL40, but not the rpL40(K22R) mutant (Extended Data Fig. 4a–c). *SMYD5* knockdown with two independent single guide RNAs (sgRNAs) led to rpL40K22me3 depletion in three different gastric cancer cell lines but had no impact on total rpL40 levels, two additional ribosomal proteins rpS6 and rpL3 or free monoubiquitin (Fig. 1j and Extended Data Fig. 4d,e). rpL40K22me3 depletion following *SMYD5* knockdown in GAC KKLS cells was also observed by targeted MS analysis of immunoprecipitated rpL40 (Fig. 1k). Furthermore, complementation of SMYD5-depleted cells with CRISPR-resistant wild-type, but not catalytically dead SMYD5(Y351A), reconstituted rpL40K22me3 levels (Fig. 1l and Extended Data Fig. 4f). Consistent with these data, the highest confidence AlphaFold Multimer model[16] placed K22 of rpL40 in the SMYD5 catalytic pocket and showed an extensive interface between the two proteins consisting of a positively charged rpL40 region nesting within a negatively charged groove on the surface of SMYD5 (Extended Data Fig. 5a,b).

Sucrose-cushion centrifugation showed that unlike rpL40, SMYD5 does not co-sediment with ribosomes. Moreover, rpL40K22me3 loss caused by SMYD5 depletion does not affect the association of rpL40 and other ribosomal proteins (the small and large subunit proteins rpS6 and rpL3, respectively) with ribosomes (Extended Data Fig. 4g). Consistent with previous reports[17], total rpL40 depletion resulted in a modest accumulation of pre-ribosomal RNAs (rRNAs) (Fig. 2a). By contrast, selective rpL40K22me3 depletion induced by *SMYD5* knockdown had no major effect on ribosome biogenesis, as evidenced by unaltered levels of several rRNA precursors compared with control (Fig. 2a). Collectively, these results indicate that the principal enzymatic function of SMYD5 is to synthesize physiological levels of rpL40K22me3. Moreover, loss of this activity does not broadly affect rpL40 ribosome association or ribosome biogenesis.

rpL40K22me3 regulates protein synthesis

Ribosome structural studies positioned rpL40 adjacent to the A site mRNA channel (Extended Data Fig. 5c). Comparisons of ribosome structures without or bound by either eEF1A or eEF2 showed that K22 of rpL40 undergoes extensive rearrangements and probably interacts with different 28S rRNA nucleotides as the ribosome cycles through elongation states (Extended Data Fig. 5d,e). Notably, rpL40 is reported to differentially associate with ribosomes in cell-specific, tissue-specific and disease-selective manners[18–22]. rpL40 is further proposed to regulate selective mRNA translation programmes, and its deletion potentially renders cells sensitive to the elongation inhibitor sordarin[20,23]. To explore whether rpL40K22 methylation per se affects mRNA translation, we performed polysome profiling experiments on extracts from KKLS and LMSU GAC control cells and from SMYD5-depleted cells[24]. An increase in the polysome to monosome (P/M) ratio was observed in both cell lines depleted of SMYD5 (and hence depleted of rpL40K22me3) relative to control cells, which was reflected by a modest accumulation of polysomes and a reduced monosome fraction (Fig. 2b,c and Extended Data Fig. 6a,b). We note that rpL40 polysome distribution with or without SMYD5 depletion mirrored the relative cognate fraction intensity (Extended Data Fig. 6c).

An increased P/M ratio may signify either an increase in initiation rates, which would increase protein synthesis, or polysome build-up due to attenuated elongation, which would manifest in reduced protein synthesis[25]. In this context, SMYD5 depletion reduced global protein synthesis in both GAC lines, as monitored through the detection of newly synthesized proteins labelled with puromycin or L-azidohomoalanine (AHA)[26,27] (Fig. 2d,e and Extended Data Fig. 6d,e). Furthermore, *rpL40* knockdown resulted in a substantial decrease in global protein synthesis (Fig. 2f). Notably, this phenotype was fully rescued by complementation with CRISPR-resistant rpL40, but only partially restored by complementation with non-methylatable rpL40(K22R) (Fig. 2f). To test whether K22me3 specifically regulates the elongation step of mRNA translation, ribosome half-transit time experiments were performed[28]. We observed that SMYD5 depletion slowed the elongation rate in KKLS cells, as the ribosome half-transit time increased by about 30% relative to control cells (Fig. 2g and Extended Data Fig. 6f). Together, these findings suggest that the SMYD5-rpL40K22me3 pathway regulates protein synthesis partially through the modulation of elongation rates, and this function is directly mediated by K22 methylation on rpL40 rather than methylation of a different hypothetical substrate (or substrates).

We next determined alterations in the transcriptome and the translatome (the pool of heavy polysome (>3 ribosome)-associated mRNAs) caused by SMYD5 depletion. Analysis of the total and heavy polysome-associated RNA sequencing data[29,30] demonstrated that SMYD5 depletion, which had little effect on the cellular transcriptome, resulted in transcription-independent differential heavy polysome association of around 1,450 distinct mRNAs (Fig. 2h and Extended Data Fig. 6g–i). Gene set enrichment analysis (GSEA) profiles of the SMYD5-dependent polysome-associated mRNA dataset showed significant overlap with oncogenic pathways, including the MYC targets signature, histone and ribosomal genes, interferon-α response pathways and gastric cancer progression-linked signatures (Fig. 2i and Extended Data Fig. 6j). Additionally, several specific mRNAs linked to gastric cancer pathogenesis and metastasis (for example, *ATF6*, *CCND1*, *CDK4*, *ERBB2*, *MAPK7*, *NRAS*, *SOX9*, *SRF* and *STAT6*, among others) were differentially associated with polysomes in a SMYD5-dependent manner (Supplementary Table 5). Direct testing of several of these targets in different GAC cell lines and a GAC patient-derived xenograft (PDX) depleted of SMYD5 showed a decrease in levels of these proteins without a change in corresponding mRNA levels (Fig. 2j and Extended Data Fig. 6k,l). This result is consistent with the idea that SMYD5 regulation occurs at the level of mRNA translation. Thus, SMYD5 may regulate gene expression at the mRNA translation level to affect GAC pathogenesis.

SMYD5 promotes GAC progression in vivo

Dysregulated protein synthesis is a common trait of rapidly proliferating cancer cells[1,2,31], which raises the possibility that SMYD5, through rpL40K22me3, influences cancer cell phenotypes. In this regard, *SMYD5* knockdown by two independent sgRNAs attenuated proliferation of four different GAC cell lines (Fig. 3a,b and Extended Data Fig. 7a–f). Additionally, the rpL40K22me3 immunohistochemistry (IHC) signal was stronger in human GAC primary and metastatic tissue samples compared with normal human stomach tissue samples (Fig. 3c), and the rpL40K22me3 signal increased significantly from normal stomach through advancing GAC stages (Fig. 3d). Total rpL40 IHC signals followed a similar pattern: strongly increasing from normal stomach to advanced GAC disease (Fig. 3d and Extended Data Fig. 7g). Despite testing several SMYD5 antibodies, we could not identify one with a specific IHC signal, which precluded the evaluation of SMYD5 expression in tissue slices. The extent of signal increase for rpL40 compared with rpS6 and rpL3 indicated the occurence of selective rpL40 upregulation in GAC rather than only a general upregulation of ribosomes (Fig. 3d and Extended Data Fig. 7h). The levels of SMYD5, rpL40K22me3 and total rpL40 levels were increased in lysates from four independent GAC cell lines compared with non-transformed IMR-90 and WI38 cell lines (Fig. 3e). Moreover, *SMYD5* knockdown did not have a major effect on global protein synthesis in IMR-90 and WI38 cells (Extended Data Fig. 7i). These observations are consistent with a potential role for SMYD5 and rpL40K22me3 in GAC neoplastic growth. Indeed, SMYD5 depletion inhibited LMSU and KKLS GAC xenograft tumour growth in vivo, and this growth was restored by complementation with CRISPR-resistant SMYD5, but not with the catalytically inactive SMYD5(Y351A) mutant (Fig. 3f and Extended Data Figs. 4g and 7j,k). Similar results were observed in a GAC PDX model in which we performed ex vivo complementation to knockdown endogenous *SMYD5* and deplete rpL40K22me3, and then reconstituted samples with either wild-type SMYD5 or the catalytically dead mutant SMYD5 (Fig. 3g,h). Finally, complementation of rpL40-depleted LMSU xenografts with wild-type rpL40 reconstituted tumour growth in vivo to control levels. By contrast, growth of xenografts reconstituted with the rpL40(K22R) mutant, which cannot be methylated by SMYD5, was substantially attenuated relative to control conditions (Fig. 3i,j). Collectively, these data implicate that SMYD5, through rpL40K22 methylation, promotes xenograft tumour growth of human GAC cell lines and PDX samples.

To directly test the in vivo role of SMYD5 in GAC pathogenesis, we established genetically engineered mouse models with high penetrance of metastatic progression to best recapitulate the natural history of the disease in humans, as two different models. The familial GAC model was based on deletion of *Cdh1*, the most common mutation found in hereditary GAC[32,33], and the spontaneous GAC model was based on common sporadic mutations in the SWI/SNF complex represented by *Arid1a* loss[5,34]. These models were combined with canonical pathways altered in GAC (*Kras*^{G12D} activation, *Trp53* deletion and *Pten* deletion) and designed to be under Cre-recombinase regulation; the familial GAC model is referred to here as *KPPC* and the spontaneous GAC model is referred to here as *KPPA* (Fig. 4a). Specific genomic regulation in the stomach was achieved by expressing Cre-ERT2 (Cre recombinase fused to a mutant oestrogen ligand-binding domain (ERT2)) under the gastric-specific *Anxa10* promoter[35], and recombination was triggered by tamoxifen administration (Fig. 4b). The *KPPC* and *KPPA* mice both developed diffuse-type gastric cancer with a mixture of signet and non-signet ring cells accompanied by marked desmoplasia and positive staining for the common human GAC hallmarks CK7 and CDX2 (ref. 36) (Extended Data Fig. 8a). Furthermore, both models showed invasion of local lymph nodes and developed other tissue metastases (Extended Data Fig. 8b). Finally, comparisons of normal stomach and GAC samples from these mice showed increased levels of SMYD5, rpL40 and rpL40K22me3, with little change in rpL3 and rpS6 levels. These results are consistent with selective mobilization of the SMYD5-rpL40K22me3 pathway in GAC (Fig. 4c and Extended Data Fig. 8c).

In parallel, Cre-conditional *Smyd5*$^{loxP/loxP}$ mutant mice were generated, which develop normally and are viable and fertile, but with tamoxifen treatment, result in specific *Smyd5* gene deletion in the stomach (Extended Data Fig. 8d,e and data not shown). In the *KPPC* background, *Smyd5* deletion (*KPPC;Smyd5*) resulted in depletion of SMYD5 and rpL40K22me3 in tissue lysates, with no impact on H3K36me3 or H4K20me3 levels (Fig. 4d). In addition, we observed complete loss of rpL40K22me3 staining in gastric cells, with attenuation of tumour cancer cell proliferation and increased apoptosis (Fig. 4e,f). Infiltration of CD45$^+$ T cells was not affected, and MYC staining was decreased (Extended Data Fig. 8f). In survival studies, *Smyd5* knockout extended the median lifespan of *KPPC* mice by around 75% (Fig. 4g). Haematoxylin and eosin (H&E) staining of tumours from *KPPC* mice showed neoplastic cell infiltration through a compromised basement membrane, whereas tumours in *KPPC;Smyd5* mice seemed contained and benign (Fig. 4e), even at the time of euthanasia (Extended Data Fig. 8g). The cause of death of *KPPC;Smyd5* mice was likely to be due to a combination of the local tumour causing physical obstruction of the gastroduodenal junction and occult bleeding secondary to structural stress and ulcerations rather than metastasis-driven morbidities (data not shown). Indeed, most of the *KPPC* mice had local lymph node invasion (6 out of 9 mice) and tissue metastases (5 out of 9 mice). By contrast, even at time of death, the *KPPC;Smyd5* mice had no detectable metastases (0 out of 9 mice) and a local lymph node signal was observed in a single mouse (1 out of 9) (Fig. 4h). Comparable results were observed in the *KPPA* model, with *Smyd5* deletion leading to an approximate 45% extension in median survival and no detection of distal metastatic disease (Fig. 4i–k and Extended Data Fig. 8h). Finally, several SMYD5-dependent polysome-associated targets were downregulated at the protein, but not mRNA level, as *Smyd5* was depleted in microdissected tissue lysates from *KPPC* tumours (Extended Data Fig. 8i,j). Together, these data implicate SMYD5 as having a key in vivo role in driving GAC progression.

SMYD5 loss sensitizes GAC to PI3K-mTOR inhibition

To test whether inhibiting the SMYD5-rpL40me3 pathway increases the effectiveness of known anticancer drugs, a comparative cell-based screen using a library assembled of 285 characterized inhibitors was performed in LMSU cells with or without SMYD5 depletion[25] (Supplementary Table 6). The top hits targeted the mTOR pathway (for example, torin 1 and everolimus), the PI3K pathway (for example, SF2523) and related pathways converging on protein synthesis regulation (for example, LY2584702 and 4EGI-1), and the strongest hit was the dual pan-PI3K-mTOR inhibitor omipalisib (Fig. 5a). In LMSU cells, SMYD5 depletion decreased the half-maximum inhibitory concentration (IC_{50}) of omipalisib by twofold (Extended Data Fig. 8k). To test for an agonistic relationship in vivo, GAC xenografts and PDX tumours with or without SMYD5 depletion were treated with omipalisib, and tumour growth was monitored. Notably, both xenograft and PDX tumour growth were inhibited by combination treatments (Fig. 5b,c). Finally, omipalisib treatment decreased global protein synthesis in LMSU cells, with SMYD5 depletion augmenting this inhibition (Fig. 5d). This result suggests that protein synthesis regulatory mechanisms potentially underlie this functional interplay.

SMYD5-based therapy for metastatic GAC

There is a high unmet need to identify new therapeutic modalities to treat peritoneal carcinomatosis (PC), the most frequent site of GAC metastases and the main cause of disease recurrence after radical gastrectomy[6,34]. To evaluate SMYD5 targeting to treat PC, we developed an in vivo model system using bioluminescence-labelled, GAC metastasis-derived and PC-forming NUGC4 cells intraperitoneally grafted[37]. Inoculated cancer cells expanded rapidly in the peritoneal cavity of NOD SCID gamma (NSG) mice, leading to mortality within 3 weeks and recapitulating the aggressive clinical behaviour of human GAC-derived PC (Fig. 5e–h). In this model, omipalisib treatment and SMYD5 depletion independently decreased PC, as reflected by significantly reduced tumour dissemination and increased median survival rates of around 65% and 40%, respectively (Fig. 5e–h and Extended Data Fig. 8i). Combining the two treatment groups substantially decreased malignant ascites and extended median survival by about 125% (Fig. 5f–h).

The widespread adoption of immunotherapies, such as immune checkpoint blockade (ICB), has transformed oncology care. Unfortunately, immune evasion due to T cell dysfunction is common in gastric cancer, which renders ICB therapies inefficient[38]. To test whether *SMYD5* deletion facilitates ICB therapies, we established a syngeneic PC allograft model utilizing cancer cells isolated from *KPPC* peritoneal metastases. In brief, *KPPC* cancer cells with or without SMYD5 depletion were implanted into the peritoneum of syngeneic mice, and grafted animals were treated with or without programmed cell death protein 1 (PD1) antibody (10 mg kg^{-1}, twice per week) and with or without omipalisib (4 mg kg^{-1}, daily), and tumour growth was monitored by bioluminescence imaging. *SMYD5* deletion and omipalisib treatment showed single-agent activity (tumour growth inhibition and lifespan extension) that was enhanced by combining the two treatments (Extended Data Fig. 9a–c). By contrast, PD1 treatment had little effect on its own or in combination with *SMYD5* deletion or omipalisib treatment (Extended Data Fig. 9a–c), which suggests that PD1 does not synergize with SMYD5 targeting.

Another strategy to overcome endogenous T cell defects is using therapies based on chimeric antigen receptor T cells (CAR-T), which deliver active cytotoxic T cells engineered to target specific cancer types[39,40]. CAR-T approaches are effective in treating several haematological malignancies and are being tested in clinical trials for patients with GAC[38,41]. However, owing to efficacy and durability challenges, CAR-T therapy will probably have most impact on GAC when coupled with other treatment strategies. To explore combining SMYD5 inhibition with immunotherapies to treat GAC, we developed a GAC-targeting adoptive transfer system using T cells expressing a CAR containing the tCD3ζ and CD28 signalling domains and the mesothelin (MSLN)-specific SS1 scFv (MSLN-CAR-T)[42], a targeting antigen commonly expressed in human GAC cells, including PC-resident cells[43] (Extended Data Fig. 9d–f). The generated MSLN-CAR-T were selectively cytotoxic to MSLN-expressing cells (Extended Data Fig. 9f). Accordingly, incubation of MSLN-CAR-T with MSLN$^+$ target cells resulted in strong CAR-T activation, as evidenced by the increased production of IFNγ, IL-2 and TNF cytokines (Extended Data Fig. 9g). *Smyd5* knockout in both normal T cells and CAR-T mouse cells exhibited no significant deleterious phenotypes (Extended Data Fig. 10a–g), and PI3K-mTOR inhibition did not interfere with the activity of CAR-T alone or in ex vivo co-culture experiments (Extended Data Fig. 10h,i). Thus, MSLN-CAR-T are functional and should not be negatively affected by treatments that target SMYD5 or the PI3K-mTOR pathways.

In vivo treatment of PC orthotopic xenografts with MSLN-CAR-T, but not control T cells, strongly inhibited tumour growth and associated lethality (Fig. 5i–l). SMYD5 depletion in NUGC4 cells provided a minor benefit for CAR-T therapy efficacy, but did not reach significance (Fig. 5j–l). Combining omipalisib with CAR-T modestly attenuated cancer dissemination and increased median survival by about 30% compared with MSLN-CAR-T treatment alone, although this was not a significant improvement compared with SMYD5 depletion in combination with CAR-T (Fig. 5j–l). Notably, combining *Smyd5* knockdown with omipalisib and MSLN-CAR-T treatment resulted in complete and durable tumour regression (Fig. 5j,k) that was accompanied by stable cancer-free survival for the entire group of mice (Fig. 5l). Additionally, no significant change in body weight was observed in the triple-therapy treatment group for the full duration of the study, a result consistent with a toxicity profile that would be well tolerated (Extended Data Fig. 10j). Collectively, our data support the in vivo functional effectiveness of MSLN-CAR-T therapy in combination with SMYD5 ablation and PI3K-mTOR inhibition for the treatment of aggressive metastatic GAC.

Discussion

Gastric cancer is a leading cause of cancer-related mortality worldwide, with some of the highest burden in Asia[4]. The lethality of GAC is largely associated with tumour dissemination to distal tissues, including the peritoneum, which highlights the importance of identifying clinically actionable targets that affect malignant evolution[6]. Our results uncovered the KMT SMYD5 as an attractive candidate (Fig. 5m). Like many KMTs, SMYD5 was initially assumed to modify histones[12]. However, we observed no evidence in vitro, in cells or in tumour tissue for such an activity. Instead, our biochemical, cellular and functional experiments provided multiple lines of evidence that rpL40K22me3 generation is the principal physiological activity of SMYD5 across diverse samples. Akin to how histone methylation regulates gene expression through transcription, we propose that rpL40 methylation regulates gene expression at the level of mRNA translation. In support of our model, SMYD5 depletion and/or rpL40K22 mutation decreased protein synthesis, and hundreds of mRNAs associated differentially with polysomes in a rpL40 methylation-dependent manner. Our data implicated the elongation step as one mechanism by which rpL40K22me3 affects protein synthesis. Future studies can explore whether other mRNA translation regulatory nodes are influenced by rpL40K22me3. During elongation, K22 undergoes conformational shifts that may alter rpL40-28S rRNA interactions within the mRNA channel, and therefore may provide a molecular explanation for the reduced elongation rate observed after SMYD5 loss. In this regard, there is growing appreciation that context-dependent dysregulation of mRNA translation influences tumorigenesis[1,2,44,45]. As several other ribosomal and elongation factors are methylated[46,47], it will be interesting to understand how crosstalk between these methylation events, and with other key ribosomal modifications[48], regulate the translatome in human health and disease.

Upregulation of *UBA52* was proposed to serve as a proxy biomarker for advancing GAC disease[49]. We observed that increased *SMYD5* expression and rpL40K22me3 signals correlated with GAC pathology, a result consistent with previous findings[8]. Future work to elucidate mechanisms of SMYD5 and rpL40 upregulation during GAC pathogenesis may uncover signalling pathways involved in the evolution of this disease. Our results leveraging in vivo GAC models provided support for a role for the SMYD5-rpL40K22me3 axis in promoting GAC malignancy. As SMYD5 seems to be largely dispensable in mice, a SMYD5 inhibitor in an oncological setting is predicted to have minimal on-target toxicity and therefore could be optimally suited for combination therapies. Indeed, the combination of SMYD5 depletion, omipalisib and CAR-T treatment cured aggressive PC in an orthotopic mouse model. From a precision medicine perspective, *SMYD5* copy gain is frequently detected in GAC (Extended Data Fig. 10k), which raises the possibility of biomarker screenings for responsive patient populations. Finally, beyond GAC, *SMYD5* chromosomal gains and upregulated expression are observed in other malignancies, including lung cancers (Extended Data Fig. 10k,l). We speculate that pathologic dysregulation of protein synthesis by the SMYD5-rpL40K22me3 pathway may have an aetiological role in these different cancer types. In summary, we identified SMYD5 trimethylation of rpL40k22 as mechanism to regulate translation elongation and to promote GAC malignant evolution. These results uncover the SMYD5-rpL40K22me3 axis as a GAC vulnerability, and potentially other neoplasms, and provide a molecular basis for the future development of SMYD5 inhibitors for the clinic.

Online content

Any methods, additional references, Nature Portfolio reporting summaries, source data, extended data, supplementary information, acknowledgements, peer review information; details of author contributions and competing interests; and statements of data and code availability are available at https://doi.org/10.1038/s41586-024-07718-0.

Methods

Plasmids

The cloning of full-length SMYD5 was based on NCBI sequence NM_006062.3. SMYD5 was cloned into a pENTR3C entry vector for subsequent cloning into a pLenti6.2/V5-DEST destination vector for mammalian protein expression in cells or into pGEX-6P-1 for recombinant protein expression in bacteria. Mutations of all proteins were generated using PfuTurbo site-directed mutagenesis (Agilent) according to manufacturer's recommendations. The SMYD5(Y351A) catalytically dead mutant was generated based on homology to other SMYD proteins[50,51]. lentiCRISPRv2 (Addgene, 52961) or lentiCRISPRv2 hygro (Addgene, 98291) were used for CRISPR-Cas9 knockouts in all cell lines.

Reagents

The following antibodies were used in this study: SMYD5 (Genemed, see below), rpL40K22me3 (Biosynth, see below), rpL40 (Abcam, ab109230), rpL3 (Bethyl Laboratories, A305-007A-T), rpS6 (Santa Cruz, sc-74459), ubiquitin (CST, 3936S), eEF1A (Millipore, 05–235), eEF2 (Abcam, ab75748), β-tubulin (Millipore, 05–661, CST, 2146S), GAPDH (CST, 2118s), puromycin (Millipore, MABE343), histone H3 (Epicypher, 13–0001), H3K36me3 (Invitrogen, MA5-24687), H4K20me3 (CST, 5737S), Vinculin (CST, 13901), ATF6 (Proteintech, 24169-1-AP), CCND1 (CST, 2978), CDK4 (Proteintech, 11026-1-AP), MAPK7 (CST, 3552), SOX9 (Proteintech, 67439-1-Ig), SRF (CST, 5147), CD45 (CST, 70257), MYC (CST, 5605), anti-mouse and anti-rabbit peroxidase conjugated antibodies (Jackson Immunoresearch, 715-035-151, 711-035-152) and peroxidase-conjugated streptavidin (Jackson Immunoresearch, NC9705430). Western blots were visualized by chemiluminescence (GE Healthcare).

Custom antibody generation

The peptide spanning rpL40K22me3 (amino acids 16–26; DKMICR(KMe3)CYAR) was synthesized and purified by high-performance liquid chromatography (>90% purity). Peptides were conjugated to KLH and used as antigen to immunize rabbits. Peptide synthesis, peptide conjugation, rabbit protocols, immunization and antiserum production were performed by Biosynth. Antiserum was negatively selected against an identical, unmodified peptide (DKMICRKCYAR). Final purification was performed with the immobilized antigenic peptide to select for methyl-specific antibodies.

GST-tag-cleaved SMYD5 protein was used as an antigen to immunize rabbits for polyclonal antibody production at Genemed Biotechnology. Antiserum was enriched for specific SMYD5 antibodies using NHS-activated high-performance columns (Sigma) following manufacturer's instructions. In brief, SMYD5 was immobilized in coupling buffer containing 200 mM $NaHCO_3$ (pH 8.3) and 500 mM NaCl. Antiserum was diluted 10-fold in dilution buffer containing 10 mM Tris (pH 7.5) and injected over the column. Specific antibodies were collected in elution buffer containing 100 mM glycine (pH 2.5).

Recombinant protein expression for in vitro reactions

Full-length cDNA of SMYD5 (NM_006062.3), UBA52 (NM_001033930.3) and fragment cDNA of SETD2 (NM_014159.7, amino acids 1417–1714) and SUV420-H1 (NM_017635.5, amino acids 62–335) were cloned into pGEX-6P-1. Lysine methyltransferases used as controls were reacted with substrates as previously reported[52,53]. Candidate substrate cDNAs were subcloned from the human ORFeome (Open Biosystems) using pGEX-6P-1. All recombinant proteins were expressed as N-terminal GST fusions from BL21 or BL21(DE3) codon plus *Escherichia coli* strain. Expression was performed at 16 °C overnight in the presence of 0.2 mM IPTG (Sigma). Recombinant GST fusions were purified with Glutathione Sepharose 4B (GE Healthcare) and eluted in 100 mM Tris pH 8.0 and 10 mg ml^{-1} reduced glutathione (Sigma-Aldrich). For the rpL40 protein tested in Fig. 1i and Extended Data Fig. 3c–e, cleavage of GST tags was performed with Prescission protease (GE Healthcare) overnight at 4 °C. cDNA of human HIV-1 tat protein was expressed as previously described[54]. In brief, C-terminal Flag-tagged tat protein expressed by transient transfection in SMYD5-depleted 293T cells was isolated from WCEs using anti-Flag M2 affinity gel (Sigma) according to the instructions of the manufacturer and eluted with 3×Flag peptides (Sigma). Histone octamers were assembled according to previously described methods[55]. Recombinant mononucleosomes (Epicypher, 16–2044) or recombinant H4K20me1 monomethyl nucleosomes (Epicypher, 16–0331) were used for enzymatic reactions for SMYD5, SETD2 and SUV420-H1 as noted. Mutations of all proteins were generated using PfuTurbo site-directed mutagenesis (Agilent) according to manufacturer's recommendations.

In vitro methylation reactions

In vitro methyltransferase reactions were performed as previously described[56] with 5 µg methyltransferase, 2 µg substrate and 2 µCi ^3H-SAM (American Radiolabeled Chemicals) or unlabelled SAM as indicated in a buffer containing 50 mM Tris pH 8.0, 20 mM KCl, 5 mM $MgCl_2$, 10% glycerol and 1 mM DTT at 30 °C overnight. Reactions were resolved by SDS–PAGE, and ^3H-methylation was visualized by autoradiography and gels were stained with Coomassie as a loading control. Reactions with deuterated SAM (C/D/N Isotopes) or regular SAM (New England Biolabs) were performed with the SAM at a final concentration of 80 µM and resolved by SDS–PAGE, followed by MS analysis or immunoblot analysis.

Preparation of WCEs

WCEs were prepared by disrupting cells in 1% NP-40 lysis buffer (50 mM Tris pH 8.0, 150 mM NaCl, 1 mM EDTA pH 8.0 and 1% NP-40, with addition of 1 mM PMSF before use). The cell resuspension was kept on ice for 10 min and then centrifuged at 14,000 r.p.m. for 10 min. Obtained WCEs were used immediately in in vitro methylation assays or for further fractionation.

Cellular fractionation

Cytoplasmic cellular extracts were prepared using established protocols[57]. In brief, cells were disrupted by hypotonic lysis (25 mM KCl, 1.5 mM $MgCl_2$, 10 mM HEPES–KOH pH 7.9 and protease inhibitors) and dounced for homogenization. Cytoplasmic extracts were then precipitated and fractionated with ammonium sulfate salt following a previously described protocol[58]. Hydrophobic interaction chromatography columns (HiTrap Phenyl FF (high sub), Cytiva)) were equilibrated in high-salt concentration of ammonium sulfate, and proteins were eluted on a reverse linear gradient from 1.4 to 0 M ammonium sulfate. Size-exclusion chromatography (Superose 6, Cytiva) was performed in hypotonic lysis buffer. Fractions were further separated by 2D gel electrophoresis according to manufacturer's recommendations (Life Technologies). Fractions were concentrated using centrifugal filter units (Amicon, 3,000 Da MWCO) before being used as substrate in in vitro reactions with radiolabelled SAM. Chromatography for substrate enrichment was performed using an AKTA FPLC (Cytiva).

SMYD5 substrate analysis by MS

In vitro methylation reactions on extracts were performed as previously described[56] using deuterated SAM as the methyl donor. The reactions were resolved by SDS-PAGE and stained using InstantBlue Protein stain (Abcam) or a SilverQuest Silver Staining kit (Invitrogen). The region around the 10 kDa band was cut into gel pieces and destained in 50% acetonitrile (ACN), 50% ammonium bicarbonate (50 mM NH_4HCO_3) for 10 min twice. Gel pieces were incubated in 50 mM NH_4HCO_3 containing 10 mM DTT at 60 °C for 30 min, followed by treatment with 50 mM iodoacetamide in 50 mM NH_4HCO_3 at room temperature for 45 min in the dark. In-gel digestion was performed using 20 ng μl^{-1} trypsin in 50 mM NH_4HCO_3 or 100 ng μl^{-1} chymotrypsin in 50 mM NH_4HCO_3 or 100 ng μl^{-1} Glu-C in 50 mM phosphate buffer (pH 7.8) at 37 °C. Two consecutive peptide extractions were processed with 5% formic acid, 49% water and 50% ACN. The resulting peptides were dried by SpeedVac, desalted using C18 StageTips (Thermo Fisher Scientific) and analysed by LC-MS/MS. Searches to identify peptides using the MaxQuant[59] software were performed with fixed modification of carbamidomethylation of cysteine and variable modifications: methionine oxidation; acetylation of protein N terminus; deuterated monomethylation, dimethylation and trimethylation of lysine; or deuterated and non-deuterated monomethylation, dimethylation and trimethylation of lysine.

Targeted MS of immunoprecipitated rpL40

For immunoprecipitation of endogenous rpL40, 1 mg of WCEs of control or SMYD5-depleted KKLS cells described in Fig. 1k or representative protein lysates of tissue biopsies described in Extended Data Fig. 8e were incubated with anti-rpL40 at 4 °C overnight and then with protein A/G magnetic beads (Pierce Protein A/G Magnetic Beads) at 4 °C for 2 h. The beads were washed with cell lysis buffer at 4 °C three times and then boiled in Laemmli buffer. The protein samples were resolved by SDS-PAGE and processed as described above for proteomics MS analysis with chymotrypsin in-gel digestion. The resulting peptides were analysed on an Orbitrap Q-Exactive mass spectrometer. Methylation states of rpL40K22 were manually inspected. Ion chromatograms for non-, mono-, di-, trimethyl peptides spanning rpL40K22 were analysed using Xcalibur Qual Browser (Thermo). The settings were as follows: peptide 19–24, *m/z* of 300.4791 (me0), 305.1509 (me1), 309.8228 (me2) and 314.4947 (me3), 10-ppm.

MS analysis

LC–MS/MS was performed using an Orbitrap Q-Exactive or Exploris mass spectrometer (Thermo Scientific) and data were manually analysed using Xcalibur Qual Browser (Thermo) or MaxQuant software.

Peptides were separated with a Vanquish Neo UHPLC system. Solvent A was 0.1% formic acid in water, and solvent B was 0.1% formic acid in ACN. The flow rate was 300 nl min^{-1}. Samples were analysed using either a 75 μm i.d. × 15 cm fused silica column (Polymicro Tech) packed with ReproSil-Pur 120 C18-AQ (3 μm, Dr Maisch) connected in line with a Thermo Q-Exactive Orbitrap mass spectrometer or a 75 μm i.d. × 15 cm C18 Easy-Spray PepMap Neo column (Thermo) connected in line with a Thermo Exploris 240 mass spectrometer.

For runs performed on the Q-Exactive, the chromatography conditions consisted of a linear gradient from 1 to 28% solvent B in 100 min, followed by 28 to 36% B in 15 min and 36 to 99% B in 0.5 min. Each MS cycle consisted of one MS1 followed by 10 data-dependent MS2 events. MS1 spectra were collected with a resolution of 70,000. HCD MS2 (NCE 27) spectra were collected with a resolution of 17,500. Dynamic exclusion was enabled with an exclusion duration of 20 s. An inclusion list was used to target the peptide KCYAR with carbamidomethylation in addition to non-methylation, monomethylation, dimethylation or trimethylation for fragmentation. For runs performed on the Exploris 240, the chromatographic conditions consisted of a linear gradient from 1 to 28% solvent B in 75 min, followed by 28 to 45% B in 10 min and 45 to 95% B in 0.5 min. MS1 spectra were acquired with a resolution of 120,000, followed by a data-dependent, 3-s cycle TopN method. HCD MS2 (HCD Collision Energy 30%) spectra were collected with a resolution of 15,000. Scan-to-scan internal mass calibration was enabled. Dynamic exclusion was enabled with a repeat count of 1 and exclusion duration of 20 s.

Western blot analysis

For western blot analysis, cells were lysed in RIPA buffer with 1 mM PMSF and complete protease inhibitor cocktail (Roche, 11873580001). Protein concentration was determined using a Bio-Rad DC Protein assay (Bio-Rad, 500–0116). Protein samples were resolved by SDS–PAGE and transferred to a PVDF membrane (0.45 μm). Dot blot analysis was performed by directly loading 1 μl of the indicated amounts of peptides onto a PVDF membrane (0.2 μm). The following antibodies were used (at the indicated dilutions): SMYD5 (1:1,000), rpL40K22me3 (1:1,000), rpL40 (1:10,000), rpL3 (1:1,000), rpS6 (1:1,000), ubiquitin (1:1,000), eEF1A (1:2,000), eEF2 (1:2,000), β-tubulin (1:2,000), GAPDH (1:5,000), puromycin (1:2,000), histone H3 (1:3,000), H3K36me3 (1:1,000), H4K20me3 (1:1,000), ATF6 (1:1,000), CCND1 (1:1,000), CDK4 (1:1,000), MAPK7 (1:2,000), SOX9 (1:1,000), SRF (1:1,000) and peroxidase-conjugated streptavidin (1:10,000). All secondary antibodies were used at 1:10,000 dilution. Protein bands were visualized using Amersham ECL or Amersham ECL Prime Western Blotting Detection reagent and quantified using ImageJ software.

Polysome profiling

Polysome profiling was performed using established protocols but with a modified buffer composition[24]. In brief, gastric cancer KKLS and LMSU cells stably expressing CRISPR-Cas9 with either sgControl or sgSMYD5 were seeded into six 15-cm Petri dishes (about 15×10^6 cells per dish) 24 h before collection of cells. Cells were treated with 100 μg ml^{-1} cycloheximide (CHX) and incubated for 5 min at 37 °C. Cells were washed twice and scraped in ice-cold PBS containing 100 μg ml^{-1} CHX, pelleted and lysed in hypotonic lysis buffer (10 mM HEPES pH 7.9, 1.5 mM $MgCl_2$, 10 mM KCl, 0.5 mM DTT, 0.5% Triton X-100, 100 μg ml^{-1} CHX, 100 U ml^{-1} RNasin inhibitor (Promega) and 1× protease inhibitor cocktail). Lysates were cleared for 10 min at 14,000 r.p.m. at 4 °C. RNA contents were determined by Nanodrop, and around 200 μg of RNA was loaded on 10–50% sucrose gradients made in 20 mM HEPES pH 7.9, 5 mM $MgCl_2$, 100 mM KCl, 100 μg ml^{-1} CHX, 100 U ml^{-1} RNasin inhibitor (Promega) and 1× protease inhibitor cocktail and prepared using a BioComp Gradient Station. Gradients were spun for 2 h in a SW 41 Ti rotor (Beckman) at 40,000 r.p.m. and 4 °C. Gradients were analysed (260 nm) and fractions collected with a BioComp Gradient Station. Obtained polysomal fractions were further used for polysome sequencing (BGI Genomics) and analysed using Anota2seq methods[29].

Polysomal RNA sequencing

Total RNA was extracted from control or SMYD5-depleted KKLS cells used in Fig. 2a ($n = 3$) using TRIzol reagent. Polysomal RNA was extracted from pooled fractions indicated as heavy polysomes. Both total RNA and polysomal RNA were subjected to polyA selection for RNA library construction. The RNA sequencing libraries were sequenced by the BGI Genomics using DNBseq platform (pair-end 100 bp analysis).

Polysomal RNA sequencing data preprocessing and quality control

BBmap[60] (v.36.59) (parameters: $k = 13$, ktrim = n, useshortkmers = t, mink = 5, qtrim = t, trimq = 10, minlength = 25) was used to trim reads for adapter sequences and low-quality base calls. In addition, the number of sequencing reads mapping to rRNA sequences obtained from the SILVA rRNA gene database[61] was calculated. The resulting reads were aligned to the human reference genome (build hg38) using HISAT2 (v.2.0.4)[62] using the '–no-mixed' and '–no-discordant' mode. The aligned reads were summarized using the 'featureCounts' function of the RSubread (v.2.6.4)[63] R/Bioconductor package (parameters: isPairedEnd = TRUE,GTF.featureType = 'exon', GTF.attrType = 'gene_id', ignoreDup = FALSE, useMetaFeatures = TRUE, countMultiMappingReads = FALSE). Reads were assigned to genes using a modified version of the RefSeq assembly GCF_000001405.40 (ref. 64) filtered to include only protein-coding genes. Principal component analysis (PCA) on TMM-$\log_2$-normalized counts (edgeR (v.3.34.1)[65], limma (v.3.48.3)[66]) was performed using the pcaMethods package (v.1.90.0)[67] (parameters: method = "svd", center=TRUE, scale = "none", eps = 0.2) (Extended Data Fig. 6e). In addition, eigen correlation plots generated with the PCAtools package (v.2.40.0) were used to assess variance explained by each principal component and correlated sources of variation (data not shown). Finally, the quality of the output files was verified using RSeQC (v.2.6.6)[68]; for example, assessing read distributions along genes to detect a 3′ or 5′ bias indicating RNA degradation (Extended Data Fig. 6f) and genomic origin of reads (data not shown).

Analysis of differential translation using the anota2seq algorithm

Genes with 0 counts in at least 1 sample were discarded, resulting in 13,481 genes being analysed. These data was TMM-$\log_2$-normalized and analysed using the anota2seq (v.1.14.0)[30] algorithm (parameters: minSlopeTranslation = −1, maxSlopeTranslation = 2, minSlopeBuffering = −2, maxSlopeBuffering = 1, deltaPT = deltaTP = deltaP = deltaT = $\log_2(1.2)$), with the addition of 'replicates' to the model to account for batch effects. Furthermore, the following thresholds were applied to identify significant changes in gene expression: min-Eff = $\log_2(1.5)$ and maxRvmPadj = 0.15 (that is, fold change > $\log_2(1.5)$ and FDR < 0.15). To classify genes into translation, buffering or mRNA abundance gene expression modes, the anota2seqRegModes function within anota2seq was used.

Quantitative PCR

RNA samples were reverse transcribed into cDNA using a SuperScript IV First-Strand Synthesis System (Invitrogen). Quantitative real-time PCR analysis was performed using a Bio-Rad CFX96 real-time PCR detection system and CFX Maestro (v.2.1) software using SYBR Green Master Mix (Invitrogen) following the manufacturer's manual and the following specific primers (5′–3′) normalized to GAPDH: hATF6-F ACCTCCTTGTCAGCCCCTAA; hATF6-R CACTCCCTGAGTTCCTGCTG; hCDK4-F GATGGCACTTACACCCGTGG; hCDK4-R GGCAGCCCAATCAGGTCAAA; hSRF-F GCCAAGCCGGGTAAGAAGAC; hSRF-R ACACATGGCCTGTCTCACTG; hCCND1-F GAGGCGGAGGAGAACAAACA; hCCND1-R GGAGGGCGGATTGGAAATGA; hSOX9-F CCCCCAACGCCATCTTCAA; hSOX9-R CTCGCTTCAGGTCAGCCTTG; hMAPK7-F GCCTATGGAGTGGTGTCCTC; hMAPK7-R AGGACCACGTAGACAGATTTGA; hGAPDH-F CGCTGAGTACGTCGTGGAGT; hGAPDH-R GTGGCAGTGATGGCATGGAC; mATF6-F GAGAGGTGTCTGTTTCGGGG; mATF6-R TGTCTGAGCAGAAGTGGCTG; mCDK4-F GTGGAGAAACCCTCGCTGAA; mCDK4-R AGGAGAGGTGGGGACTTGTT; mCCND1-F GAGCCCAACCGAGACCAC; mCCND1-R CTTCGCACTTCTGCTCCTCA; mSRF-F ATCACCAACTACCTGGCACC; mSRF-R TCACAGCCATCTGGTGAAGC; mSOX9-F TGAAGATGACCGACGAGCAG; mSOX9-R GGATGCACACGGGGAACTTA; mMAPK7-F TGAAGCCTACTGTGCCCTATG; mMAPK7-R TGATCTGGTGTAGGTCGCTC; and mGAPDH-F CAACTTTGGCATTGTGGAAGGG; mGAPDH-R ACACATTGGGGGTAGGAACAC.

GSEA

Genes identified as differentially associated with polysomes by anota2seq analysis (that is, transcripts with increased or decreased association with polysomes without corresponding changes in total mRNA levels) were selected for GSEA[69,70] using the R fgsea package (v.1.24.0)[71]. NES and nominal *P* values were calculated as previously described[69,70]. Enrichment analysis was performed for Hallmark, KEGG and curated pathways.

Translation assays

Puromycylation assays were performed as previously described[26] in control or SMYD5-depleted KKLS and LMSU cells. Cells were seeded at 3–4 × 10^5 cells in 6-well plates 24 h before collection. Puromycin pulses were performed by incubating the cells with 10 μg ml^{-1} puromycin for 15 min at 37 °C. Cells were then washed with ice-cold PBS and lysed in RIPA buffer supplemented with protease inhibitor mixture. Next, 5 μg of whole cell lysates were assayed by western blot analysis using the anti-puromycin antibody to capture newly synthesized protein.

AHA labelling of newly synthesized proteins was performed as previously described[25] in control or SMYD5-depleted KKLS and LMSU cells. Cells were seeded at 3–4 × 10^5 cells in 6-well plates 24 h before collection. Cells were maintained in methionine-free RPMI for 1 h, then grown in RPMI containing 50 μM AHA for 2 h. Cells were treated with 100 μg ml^{-1} CHX and incubated for 5 min at 37 °C. Cells were washed twice with ice-cold PBS containing 100 μg ml^{-1} CHX and lysed in RIPA buffer. Click reactions were performed using a Click Chemistry Reaction Buffer kit (Vector Laboratories, CCT-1001) following the manufacturer’s protocol. In brief, 100 mg of WCEs were incubated with 40 μM Biotin-PEG4-Alkyne for 30 min. The proteins were extracted with methanol and chloroform and 1–5 mg was assayed by western blot analysis using peroxidase-conjugated streptavidin.

Measurement of ribosome half-transit time

Ribosome half-transit time was determined as previously described[72] with the following modification. In brief, control or SMYD5-depleted KKLS or LMSU cells (3–4 × 10^5 cells) were starved for 10 min in Met/Cys-free RPMI medium supplemented with 10% dialysed FBS, and then 10 μCi ml^{-1} of $[^{35}S]$Met/Cys (EXPRESS$[^{35}S]$, Revvity) was added. At the times indicated (2.5, 5 and 10 min), 100 μg ml^{-1} CHX was added, cells were washed twice and scraped in ice-cold PBS containing 100 μg ml^{-1} CHX. Cells were pelleted and lysed in 200 μl of ribosome suspension buffer (10 mM NaCl, 10 mM Tris pH 7.4, 15 mM $MgCl_2$, 1% Triton X-100 and 1% NP-40) supplemented with protease inhibitor mixture and incubated on ice for 15 min with sporadic vortexing. Nuclei and mitochondria were pelleted by centrifugation for 10 min at 20,800*g* at 4 °C. Next, 200 μl of post-mitochondrial supernatant was mixed with an equal volume of polysomal buffer (25 mM Tris pH 7.4, 10 mM $MgCl_2$, 25 mM NaCl, 0.05% Triton X-100 and 0.14 M sucrose) with protease inhibitor mixture, and 180 μl was removed to measure incorporation of $[^{35}S]$ Met/Cys into total protein (nascent and completed). The remaining supernatant was centrifuged at 100,000 r.p.m. (Beckman TLA 100.1) for 1 h at 4 °C to pellet down polysomes. Next, 180 μl of post-ribosome supernatant was removed to measure the incorporation of $[^{35}S]$Met/Cys into completed protein. Post-mitochondrial supernatant and post-ribosome supernatant samples were mixed with equal volumes of 20% TCA containing 20 μg ml^{-1} BSA, placed on ice for 20 min, and the proteins were pelleted by centrifugation for 5 min at 20,000*g* at 4 °C. The TCA protein precipitates were washed twice with ice-cold acetone and dissolved in 100 μl of 1% SDS-supplemented RIPA (50 mM Tris pH 7.4, 150 mM NaCl, 2 mM EDTA, 1% NP-40 and 1% SDS). Samples were moved to 5 ml of Ultima Gold (Revvity) and allowed to sit for 30 min at room temperature and subjected to liquid scintillation counting.

Ribosome biogenesis (northern blotting)

Total RNA from control, SMYD5-depleted or rpL40-depleted KKLS cells was extracted using TRIzol (Invitrogen, 15596018) according to the manufacturer's instructions and resuspended in formamide. Extracted RNA (6 µg) was resolved on 1% agarose–formaldehyde gels in tricine–triethanolamine (TT) as previously described[73], after adding equal volumes of freshly made loading dye (0.4 M formaldehyde, 1× TT buffer, 0.5 mM EDTA and 0.02 % bromophenol blue) and incubating at 70 °C for 5 min. Electrophoresis was performed in 1× TT buffer and stopped when the bromophenol blue dye front reached around three-quarters of the gel length. Uneven edges and wells of the gel were cut off, and overnight capillary transfer using 20× SSC buffer (3.0 M NaCl and 0.3 M sodium citrate, pH 7.0) was established to transfer the RNA onto a nylon membrane (Cytiva, RPN303B), cut to exact size. RNA was UV crosslinked to the membrane (CL-1000 UV Crosslinker) using $1{,}200 \times 100\ \mu J\ cm^{-2}$ and visualized after staining with methylene blue (0.03% methylene blue, 0.3 M sodium acetate, pH 5.2). Destaining was achieved through successive washes with 1× SSC and 0.1% SDS. Subsequently, 50 ml of hybridization buffer was freshly made by mixing 15 ml 20× SSPE (Ambion, AM9767), 2.5 ml 100× Denhardt's solution (Biobasic, D0062), 1 ml herring sperm DNA (Invitrogen, 15634017) denatured at 95 °C for 10 min, 30.5 ml nuclease-free water, 1 ml 10% SDS and heated to 65–70 °C. The membrane was immediately covered with hybridization buffer and incubated for 1 h at 37–42 °C. Oligonucleotide probes were fluorescently labelled days before as previously described[74] and stored at −20 °C, in the dark. DNA oligonucleotide probes of desired sequence (probe 5520, 5′- CCTCGCCCTCCGGGCTCCGTTAATGATC-3′, targeting 5′ITS1 region as previously described[75], were ordered from Integrated DNA Technologies, with primary amine groups at both termini. Probe labelling was performed by vigorously mixing 50 µg of DyLight 800 NHS Ester (Thermo Scientific, 46422) with 10 µg of amine-modified oligonucleotide (resuspended in 20 µl of 100 mM sodium carbonate, pH 9.0, following complete drying in a vacuum concentrator, Savant, SpeedVac Plus SC110A), and incubating in the dark, overnight, at room temperature. The following day, fluorescently labelled oligonucleotides were retrieved using a QIAquick Nucleotide Removal kit (Qiagen, 28306), according to the manufacturer's instructions, with minor modifications (re-loading sample on the same column again after first flow-through, and washing twice afterwards), and resuspended in 100 µl of elution buffer. Detection of precursor rRNA forms was achieved through spiking 20 pmol of fluorescently labelled oligonucleotide probes into the hybridization buffer while making sure to briefly remove and thoroughly mix the buffer and probe before covering the membrane again to start hybridization. Incubation with the labelled probe was done overnight at 42 °C, with constant agitation and protection from light. The membrane was then washed twice with 2× SSC, 0.1% SDS and once with 1× SSC, 0.1% SDS, each wash with constant agitation, for 10 min, at 45 °C. Northern blots were developed through near-infrared fluorescence imaging (Azure Biosystems, c600), by exposing for about 30–60 s.

AlphaFold prediction of UBA52 and SMYD5 structure

Structural prediction of UBA52 and SMYD5 was generated using AlphaFold (v.2.3), downloaded and installed on a local computing cluster. Predictions used the 'multimer' prediction mode[76]. FASTA files of the reviewed canonical isoforms of UBA52 and SMYD5 were obtained from UniProt, concatenated and provided as input to AlphaFold. Full sequence databases were queried for the MSA search step using AlphaFold’s default pipeline. AlphaFold’s default multimeric modelling was used for structural prediction, generating 5 predictions each using 5 AlphaFold models, producing 25 total predictions. Each of the resulting predictions were ranked by AlphaFold’s default quality metric for multimers (PTM+iPTM score). The top-ranking prediction was visualized and labelled using ChimeraX.

Cell culture

HEK-293T (American Type Culture Collection (ATCC), CRL-1573) and U2OS (ATCC, HTB-96) cells were cultured in Dulbecco’s modified Eagle’s medium (DMEM, Life Technologies) supplemented with 10% FBS, 2 mM L-glutamine and penicillin–streptomycin (Life Technologies). A549 (ATCC, CCL-185; oncogenic mutations: *KRAS*^{G12S}, *STK11*^{Q37*}, *KEAP1*^{G333C}, *SMARCA*^{4Q729Cfs*4} and *CTNNA1*^{E865*}), KKLS (CVCL_1B37; amplification of 8q (*MYC*) and *p53*^{Del}), NCI-N87 (ATCC, CRL-5822; *p53*^{R248Q}; *p53*^{Del}; *ARID1A*^{Del}; *PBRM1*^{Del}; *KMT2C*^{Del}; *ERBB2*^{Amp}; *MYC*^{Amp}), NUGC4 (RIKEN, RCB1939; *CDH1*^{D257V}; *CDKN2A/B*^{Del}; *ATM*^{Del}; *PBRM1*^{Del}; *BAP1*^{Del}; *ERBB2*^{Amp}; *EGFR*^{Amp}; *MET*^{Amp}; *JAK2*^{Amp}; *RAC1*^{Amp}) and SH10TC (RIKEN, RCB1940; *KRAS*^{G12V}; *PTEN*^{N12Kfs32}; *p53*^{R273C}; *ARID2*^{C811*}; *CDKN2A/B*^{Del}; *SMAD4*^{Del}; *SMARCA2*^{Del}; *RB1*^{Del}; *MYC*^{Amp}; *KRAS*^{Amp}) cells were grown in RPMI 1640 medium supplemented with 10% FBS, 2 mM L-glutamine and penicillin–streptomycin (Life Technologies). AGS (ATCC, CRL-1739; *KRAS*^{G12D}; *PIK3CA*^{E545A}; *CDH1*^{G579Rfs*9}; CTNNB1^{G34E}; *ARID4Aq*^{1087Afs*15}; *ep300*$^{E643*/E1025*}$; *CDH1*^{Del}; *SMAD4*^{Del}; *AKT2*^{Amp}; *CCNE1*^{Amp}; *AXL*^{Amp}) cells were grown in Ham’s F12K medium supplemented with 10% FBS, 2 mM L-glutamine and penicillin–streptomycin (Life Technologies). LMSU (RIKEN, CVCL_4849; *p53*^{R175H}; *ERCC2*^{*761Sext*7}; *CDKN2A/B*^{Del}; *SMARCA2*^{Del}; *FGFR1*^{Amp}; *MYC*^{Amp}; *RICTOR*^{Amp}; *YAP1*^{Amp}; *RAC1*^{Amp}; *CCND1*^{Amp}; *MERTK*^{Amp}) cells were grown in Ham’s F-10 medium supplemented with 10% FBS, 2 mM L-glutamine and penicillin–streptomycin (Life Technologies). All above cell lines were authenticated and declared mycoplasma-free by ATCC.

Transfection and viral transduction

Transfections were performed with either TransIT-293 or TransIT-LT1 (Mirus, MIR-2706) in 293T cells. Stable cell lines were generated using lentiviral transductions. 293T cells were co-transfected with lentiviral plasmid, pCMV-Δ8.2 (Addgene, 8455) and pCMV-VSVg (Addgene, 8454) in a ratio of 5:4:1 by mass. At 48 h after transfection, target cells were transduced with 0.45 μm filtered viral supernatant supplemented with 4 μg ml^{-1} polybrene. Viral concentration was performed, if necessary, with Lenti-X lentiviral concentration solution per the manufacturer’s recommendations (Takara, 631232). Cells were selected 24 h after medium replacement with 2 μg ml^{-1} puromycin (Thermo, A1113802) for cell lines used for substrate screening or 250 μg ml^{-1} hygromycin B (Corning, 30240CR) for other cell lines. To deplete SMYD5 in cells, a CRISPR-Cas9 system was used with lentiCRISPRv2 (Addgene, 52961) or lentiCRISPRv2 hygro (Addgene, 98291) with the following sgRNAs: sgControl (called sgSafe), 5′-GGGCTACTAGGATTCAATCT-3′; sgSMYD5-1, 5′-AATGCACTTTATCGCTACCG′; sgSMYD5-2, 5′-CATCTTC GTAGAACGGCCCC-3′. For SMYD5 reconstitution experiments, stable integration of SMYD5 was achieved through lentivirus-mediated incorporation using pLenti6.2 V5-DEST construct (Thermo, V36820) cloned with *SMYD5* cDNA. Following incorporation, a selection process was performed using 10 μg ml^{-1} blasticidin (Thermo, R21001). To ensure the stability of the incorporated exogenous *SMYD5* cDNA, sgSMYD5-1, of which targeting the exon–intron junction of *SMYD5*, was used in the reconstitution experiments.

Cell assays

For cell proliferation assays, cells were seeded at 2×10^5 cells per ml in triplicate in 6-well plates. Cell counts were acquired using a Countess III FL Automated Cell Counter (Thermo Fisher Scientific) at indicated days for 8 days. After each counting, the cells were maintained at a density of $2–4 \times 10^5$ cells per ml. Trypan blue was used to stain non-viable cells. Cell numbers were expressed relative to 1×10^5 cells per ml.

Cell drug screening was performed as previously described[25]. In brief, sgControl and sgSMYD5 LMSU cells were seeded at 5×10^3 cells per ml in triplicate in 96-well plates. Cells were then subjected to treatment with a drug library (50 nM; Supplementary Table 6) or DMSO (vehicle control). The viability of treated cells was measured using a live cell kinetic imaging system (CellCyte, Discover Echo) for 120 h with data collection every 4 h. Data are represented as the mean ± s.e.m.

For evaluation of PI3K-mTOR inhibitor sensitivity, the IC_{50} of omipalisib was measured with or without SMYD5 depletion in GAC cell culture assays. LMSU cells were plated at density of 5,000 cells per well in 96-well plates using a Multichannel pipette (Rainin) and allowed to attach for at least for 6 h. Cells were then treated with a dilution series of the drug and grown for 72 h. Cell viability assay was performed using PrestoBlue HS cell viability reagent (Thermo, P50201). Data were obtained as mean ± s.e.m of three technical replicates in two independent experiments. The IC_{50} value was calculated using GraphPad Prism 9.5 software.

TCGA dataset analysis

TCGA data from patients with GAC (project identifier: TCGA-STAD, dbGaP study accession: phs000178)[77] and other indicated cancer types were analysed using cBioPortal (v.5.3.13)[78,79] to identify *SMYD5* mutations, copy number variations and mRNA expression. Copy number gain datasets within the portal were generated by the genomic identification of significant targets in cancer (GISTIC) algorithm to identify significantly altered regions of amplification or deletion across sets of patients. Basal-normalized transcript expression data (z scores) used for this analysis were RNA Seq V2 RSEM.

Histology and immunohistochemistry

Tissue specimens were fixed in 4% buffered formalin for 24 h and stored in 70% ethanol until paraffin embedding. Sections (3 μm) were stained with H&E or used for immunostaining studies. Tissue microarray patient specimens were collected after written consent from the patients and in accordance with the institutional review board-approved protocols of the University of Texas MD Anderson Cancer Center (MDACC; PA19-0435, principal investigator (PI): P.K.M.). The following antibodies were used (at the indicated dilutions): cleaved caspase-3 (CST, 9664; 1:200); CD45 (CST, 70257; 1:500); MYC (CST, 5605; 1:500); Ki67 (550609 BD Bioscience; 1:1,000); rpL40 (Abcam, ab109230; 1:400); rpL40K22me3 (Biosynth, 1:2,000; see custom antibody generation); rpL3 (Proteintech, 11005-1-AP; 1:250); and rpS6 (CST, 2217). IHC was performed on formalin-fixed, paraffin-embedded tissue sections using a biotin–avidin HRP conjugate method (Vectastain ABC kit) as described before[80]. Sections were developed with DAB and counterstained with haematoxylin. Pictures were taken using a PreciPoint M8 microscope equipped with the PointView software and quantified using ImageJ software.

Animal models

Kras$^{+/LSL\text{-}G12D}$, *Trp53*$^{loxP/loxP}$, *Pten*$^{loxP/loxP}$, *Cdh1*$^{loxP/loxP}$, *Arid1a*$^{loxP/loxP}$ and Anxa10-cre^{Ert2} mice have been described before[35,81–85]. Reporter-tagged insertion with conditional potential *Smyd5*$^{tm1a(EUCOMM)}$ mouse strain was obtained from the European Mouse Mutant Archive repository[86]. In brief, the *Smyd5*$^{tm1a(EUCOMM)}$ targeted knock-in sequence includes the Neo-LacZ cassette flanked by *Frt* sites and exon 2 sequence flanked by *loxP* sites. Founder mice were crossed with *Rosa26*^{FlpO} deleter strain[87] to generate conditional allele *Smyd5*$^{loxP/loxP}$. Mice were maintained on a mixed C57BL/6;129S1 strain background and we systematically used littermates as controls in all the experiments. Immunocompromised female NSG mice (*NOD.SCID-IL2Rg*$^{-/-}$) were utilized for transplantation studies. All experiments were performed on 6-10-week-old female animals. All animals were numbered, and experiments were conducted in a blinded fashion. After data collection, genotypes were revealed, and animals were assigned to groups for analysis. For treatment experiments, mice were randomized. None of the mice with the appropriate genotype were excluded from this study or used in any other experiments. All mice were co-housed with littermates (2–5 per cage) in pathogen-free facility with standard controlled temperature of 22 °C, with a humidity of 30–70% and a light cycle of 12 h on/12 h off set from 7:00 to 19:00 and with unrestricted access to standard food and water under the supervision of veterinarians in an AALAC-accredited animal facility at the MDACC. Mouse handling and care followed the NIH Guide for Care and Use of Laboratory Animals. All animal procedures followed the guidelines of and were approved by the MDACC Institutional Animal Care and Use Committee (IACUC protocol 00001636, PI: P.K.M.). Tumour size was measured using a digital caliper, and tumour volume was calculated using the following formula: volume = $(\text{width})^2$ × length/2, where length represents the largest tumour diameter and width represents the perpendicular tumour diameter. The end point was defined as the time at which a progressively growing tumour reached 20 mm in its longest dimension as approved by the MDACC IACUC protocol (00001636, PI: P.K.M.); in no experiments was this limit exceeded.

GAC mouse models

To model GAC development, we crossed gastric epithelium-specific Cre strain *Anxa10*^{creErt2} with mice carrying the conditional mutant alleles *Kras*$^{+/LSL\text{-}G12D}$*, Trp53*$^{loxP/loxP}$*, Pten*$^{loxP/loxP}$, *with Cdh1*$^{loxP/loxP}$ (*KPPC*) or *Arid1a*$^{loxP/loxP}$ (*KPPA*). To study the role of SMYD5 in gastric tumorigenesis, the *KPPC and* KKPA models were crossed with conditional *Smyd5*$^{loxP/loxP}$ mutant (*KPCS;Smyd5*). To induce Cre recombination and initiate tumorigenesis, animals were intraperitoneally injected with 1 mg tamoxifen (Sigma-Aldrich) diluted in 100 μl sunflower oil at 8 weeks of age. For tumour development studies, animals were killed at 6 weeks after tamoxifen injection and tissues were processed for biochemical, histological and immunohistochemical analyses. Tumour biopsies were collected, and protein lysates were prepared to confirm the mutation of conditional alleles by immunoblotting. For survival studies, mutant mice were continuously monitored for signs of disease progression. At morbidity, tumours were processed for biochemical, histological and immunohistochemical analysis.

Xenograft models and treatment studies

PDX were obtained from the NCI Patient-Derived Models Repository, NCI-Frederick, Frederick National Laboratory for Cancer Research (specimen identifier: 197837-219-T). A tumour specimen from the lymph node metastatic site was obtained from the de-identified patient (female, 56 years old) with histologically confirmed GAC received before treatment carboplatin–paclitaxel, epirubicin–oxaliplatin and carboplatin–docetaxel therapy for 6 months with disease progression. Whole exome sequencing analysis revealed that the PDX carries characteristic GAC mutations, specifically *CDH1*^{A617T} and *TP53*$^{X307\_splice}$. PDX tumour specimens were collected after written patient consent and in accordance with the institutional review board-approved protocols of the MDACC (PA19-0435, PI: P.K.M.).

For omipalisib therapy studies, PDX specimens and 2 × 10^6 NLMSU cells were grafted subcutaneously to NSG mice. When tumours became palpable, they were calipered to monitor growth kinetics. Mice were treated as indicated with omipalisib (4 mg kg^{-1} once per day, intraperitoneally) in vehicle 40% (2-hydroxypropyl)-β-cyclodextrin. Control animals underwent the same procedure but received vehicle treatment. For xenograft mouse model of GAC PC, we utilized the NUGC4 GAC metastatic cell line. Cells were lentivirally transduced to express luciferase reporter and intraperitoneally injected (1 × 10^6) into NSG mice. Mice were treated as indicated with a single dose of MSLN-CAR-T (2 × 10^6) injected into the peritoneal cavity as indicated and/or omipalisib (4 mg kg^{-1} once per day, intraperitoneally) in vehicle 40% (2-hydroxypropyl)-β-cyclodextrin. Control and monotherapy animals underwent the same procedure but received mock T cells and vehicle treatment. To monitor cell growth, mice were intraperitoneally injected with 30 mg kg^{-1} d-Luciferin (Sigma-Aldrich) in 100 μl 0.9% NaCl. Immediately after substrate injection, bioluminescent images were acquired in an AMI HTX bioluminescence imaging system (Spectral Instruments Imaging). Imaging settings were as follows: emission filter, open; field of view, 25 cm; f-stop 1.2; low binning 2 × 2 and exposure time, 30 s. X-ray imaging camera settings were as follows: field of view, 25 cm; low exposure and high resolution. Images were analysed using Aura software (Spectral Instruments Imaging) and quantified in radiance units of photons per second per square centimetre per steradian (photons s^{-1} cm^{-2} sr^{-1}).

Syngeneic PC model

To test the efficacy of PD1 therapy, a syngeneic PC allograft model was established in C57BL/6;129S1 mice from cancer cells isolated from *KPPC* peritoneal metastases.

KPPC cells were transduced with lentiviral vectors to express luciferase reporter and Cas9–sgControl or sgSMYD5 and implanted (2×10^5) into the peritoneum of syngeneic mice. Animals were treated with or without PD1 (10 mg kg^{-1}, twice per week) and with or without omipalisib (4 mg kg^{-1}, daily). Control groups received placebo (vehicle) treatment. Tumour growth was monitored by bioluminescence imaging as described above using an AMI HTX bioluminescence imaging system (Spectral Instruments Imaging).

CAR-T generation and analysis

Codon-optimized sequences for truncated human nerve growth factor receptor (tNGFR), a cell surface reporter, self-cleaving P2A peptide sequence and SS1-28z (MSLN) CAR[42] were synthesized (Twist Bioscience) and cloned in tandem downstream of the *eEF1A* promoter of PCDH lentiviral plasmid (Clontech) using Gibson Assembly (NEB). For lentivirus production, 293T cells were transfected with the PCDH-MSLN-CAR-T, psPAX2, PM2G plasmids at a ratio of 10:6.5:3.5 with PEI. The virus-containing supernatants were collected 48 h later, centrifuged at 4,000*g* to remove the cell debris, filtered through the 0.45 µm pore-sized membrane and centrifuged at 20,000*g* for 2 h at 4 °C to concentrate viral particles. The virus pellet was resuspended in complete T cell medium: RPMI-1640 supplemented with 10% FBS, 10 mM HEPES, 10 mM sodium pyruvate, 1× non-essential amino acid, 50 units per ml penicillin and 50 µg ml^{-1} streptomycin, 50 µM β-mercaptoethanol, 100 units per ml human IL-2 (Thermo Fisher). The concentrated lentivirus was used immediately or stored at −80 °C. Healthy donor-derived peripheral blood mononuclear cells (PBMCs) were isolated by Ficoll-Paque PLUS density gradient centrifugation (GE Healthcare). PBMCs were collected in accordance with the institutional review board-approved protocols of the MDACC (PA19-0435, PI: Mazur). PBMCs were activated with CD3/CD28 Dynabeads (Gibco) at a 1:5 cell to beads ratio in T cell medium. At 24 h later, PBMCs were transduced with concentrated lentivirus expressing MSLN-CAR-T (multiplicity of infection = 10) with 10 µg ml^{-1} polybrene. At 72 h after the initial stimulation, beads were removed, and the cells received fresh T cell complete medium and were cultured for another 3 days at 1×10^6 cells per ml density. The CAR-T transduction rate was quantified by NGFR reporter and Fab staining (Jackson ImmunoResearch Lab). Cells were analysed using an Attune NxT flow cytometer (Thermo Fisher) and FlowJo (v.10) software.

MSLN-CAR-T effector function was evaluated by MSLN-specific lysis by co-culture assays with $MSLN^+$ and $MSLN^-$ target cells. To that end, NALM6 cells were transduced to express MSLN or unrelated marker (GD2) and luciferase reporter. MSLN and GD2 expression was confirmed by immunostaining followed by analysis using an Attune NxT flow cytometer (Thermo Fisher). MSLN-CAR-T or mock T cells were co-cultured with MSLN-NALM6 and GD2-NALM6 cells at indicated effector to target (E:T) ratio. Luciferase reporter signal was assessed (Promega) using a luminometer (Synergy H1, Biotech) at indicated time points, and the relative cell viability was calculated as the percentage of the control cell luciferase signal. To test MSLN–CAR-T cytotoxic activity on gastric cancer cells, we first validated by flow cytometry that all utilized target cancer cells showed cell surface expression of MSLN. Next, cancer cells were transduced with luciferase reporter and co-cultured with CAR-T in triplicate with the indicated E:T ratio. The luciferase reporter signal was measured as described above. Control and single-therapy cancer cells received mock T cells and vehicle treatment.

For intracellular cytokine staining analysis, CAR-T and target cells were co-cultured at a 1:1 ratio for 6 h. Next, 10 μM monensin was added after 4 h of co-culture. After incubation, MSLN–CAR-T were prepared for intracellular staining using a Fixation/Permeabilization kit (BD Biosciences) according to the manufacturer's instructions. In brief, the cells were first stained with surface markers then fixed and permeabilized. Intracellular cytokines IFNγ, TNF and IL-2 were then detected using specific antibodies: IL-2-PECy7 clone MQ1–17H12, IFNγ-APC/Cy7 clone 4 S.B3 and TNF-BV711 clone Mab11 (BioLegend). Cells were washed and resuspended in flow buffer (PBS + 0.5 mM EDTA + 0.5% BSA) and analysed using an Attune NxT flow cytometer (Thermo Fisher).

Quantification and statistical analysis

Please refer to the figure legends or the experimental details for description of sample size (n) and statistical details. All values for n are for individual mice or individual sample. Sample sizes were chosen based on previous experience with given experiments. Cell culture assays were performed in triplicate and in two independent experiments unless stated otherwise. Data are expressed as the mean ± s.e.m. Differences were analysed by log-rank, two-tailed t-test, two-way ANOVA with Tukey testing for multiple comparisons using GraphPad Prism 9.5. P values ≤ 0.05 were considered significant. Western blot signals were quantified using ImageJ (1.53k).

Statistics and reproducibility

All statistics used in this study are described when used in the appropriate section. For all the western blot, autoradiography and cell culture assay results, the reported data were reproduced three independent times (or more as indicated), the reported data were reproduced three independent times (or more as indicated) and representative data are shown. No statistical methods were used to predetermine sample sizes. GraphPad Prism 9.5 software or Microsoft Excel 2023 was used for statistics calculation.

Reporting summary

Further information on research design is available in the Nature Portfolio Reporting Summary linked to this article.

Extended Data

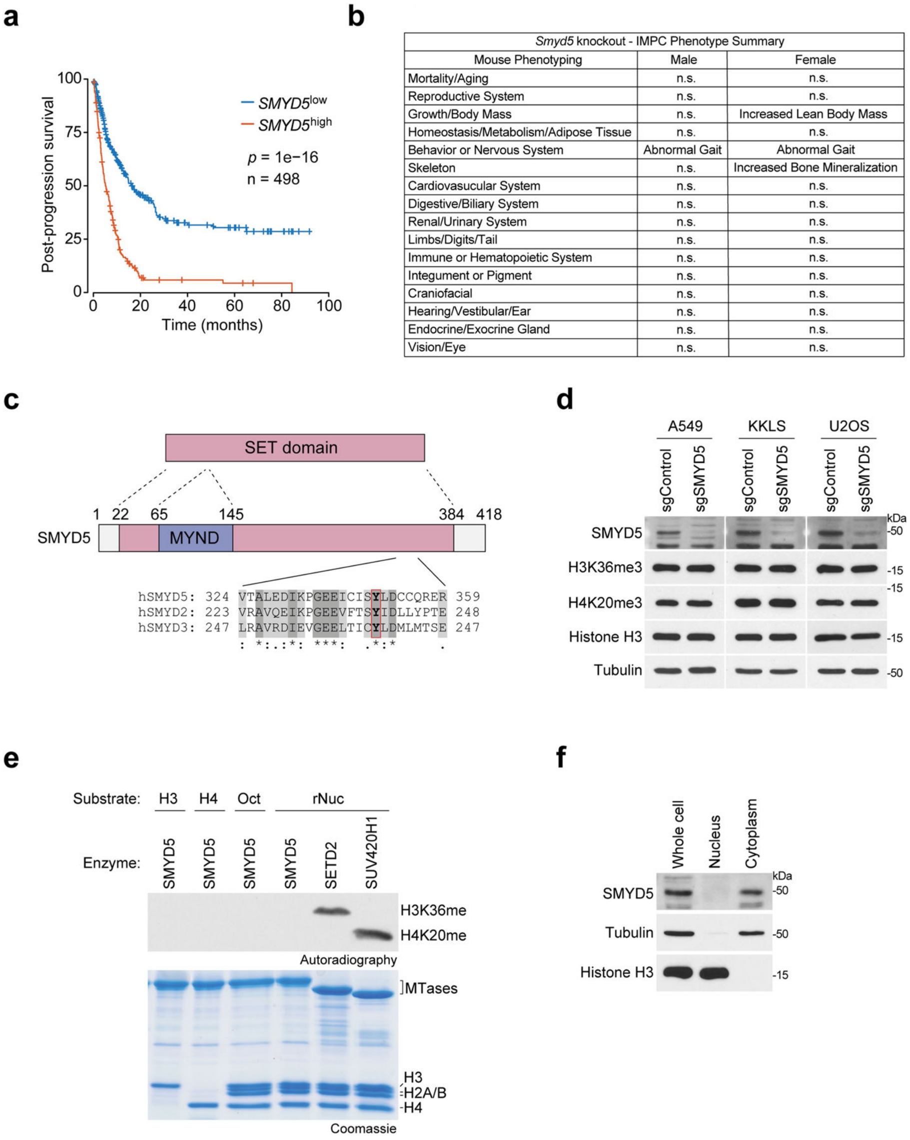

Smyd5 knockout - IMPC Phenotype Summary		
Mouse Phenotyping	Male	Female
Mortality/Aging	n.s.	n.s.
Reproductive System	n.s.	n.s.
Growth/Body Mass	n.s.	Increased Lean Body Mass
Homeostasis/Metabolism/Adipose Tissue	n.s.	n.s.
Behavior or Nervous System	Abnormal Gait	Abnormal Gait
Skeleton	n.s.	Increased Bone Mineralization
Cardiovasucular System	n.s.	n.s.
Digestive/Biliary System	n.s.	n.s.
Renal/Urinary System	n.s.	n.s.
Limbs/Digits/Tail	n.s.	n.s.
Immune or Hematopoietic System	n.s.	n.s.
Integument or Pigment	n.s.	n.s.
Craniofacial	n.s.	n.s.
Hearing/Vestibular/Ear	n.s.	n.s.
Endocrine/Exocrine Gland	n.s.	n.s.
Vision/Eye	n.s.	n.s.

Extended Data Fig. 1 |. SMYD5 is largely dispensable in mice and there is no evidence for SMYD5 having histone methylation activity in vitro or in cells.

a, *SMYD5* expression levels in gastric cancer negatively correlate with GAC patient progression free survival (n = 498 patients). *P*-values determined by log-rank test. **b**, Summary of full embryonic *Smyd5* knockout mice phenotype data from the IMPC (International Mouse Phenotyping Consortium). *Smyd5* deletion has no impact on viability and fertility and mice have only minor phenotypes as shown in the table. **c**, Top, main domain structure of SMYD5. SMYD5, like the four other SMYD family members (SMYDs 1–4), contains a catalytic methyltransferase SET domain that is disrupted due to insertion of a MYND domain. When the protein folds, the two parts of the SET domain form a continuous functional domain as shown. Bottom, alignment of the putative catalytic region of SMYD5 with the catalytic regions of SMYD2 and SMYD3. Grey box, homology, or similarity. Red box, catalytic tyrosine in SMYD2 and SMYD3 that was used to generate a catalytic mutant for SMYD5. **d**, SMYD5 depletion has no effect on the levels of H3K36me3 and H4K20me3 in three different human cell lines. Western blots with the indicated antibodies of WCEs from control or SMYD5-depleted A549, KKLS, and U2OS cells. Total H3 and tubulin are shown as loading controls. **e**, SMYD5 does not methylate free histones, octamers, or nucleosomes in vitro. In vitro methylation assays with the indicated enzymes and substrates. H3: free histone H3; H4: free histone H4; Oct: recombinant octamers (2 each of H2A, H2B, H3 and H4); rNuc: recombinant nucleosome. SETD2 and SUV420H1 are included as positive controls for methylation of H3K36 and H4K20, respectively. Note that SUV420H1's preferred substrate is H4K20me1 nucleosome and as indicated, H4K20me1 nucleosomes were used in the SUV420H1 methylation assays. Top panel, ^{3}H-SAM was used as methyl donor and the methylation was visualized by autoradiography. Bottom panel, Coomassie stain of proteins present in the in vitro reactions. **f**, SMYD5 localizes to the cytoplasm. Western blots with the indicated antibodies of biochemically separated 293 T WCEs into nuclear and cytoplasmic fractions. Tubulin and H3 are shown as controls for the integrity of the fractionation with Tubulin exclusively present in cytoplasmic fractions and H3 exclusively present in nuclear fractions.

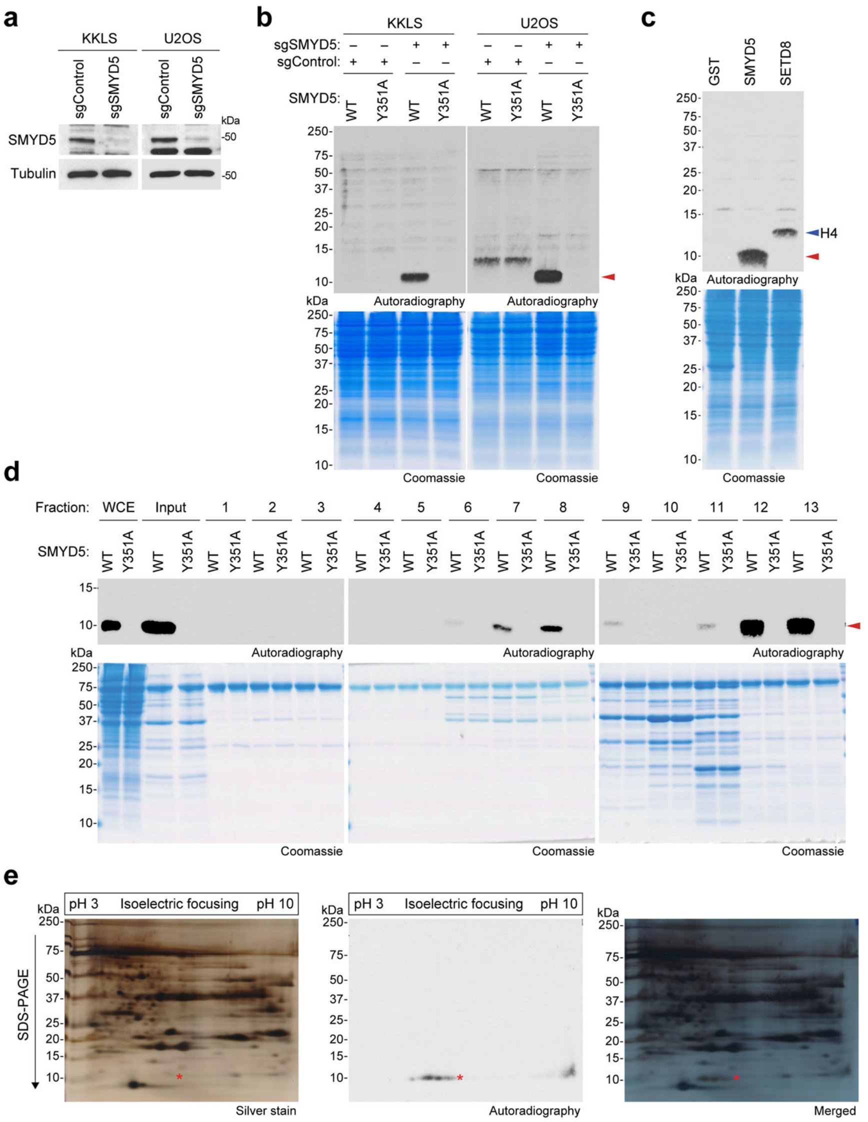

Extended Data Fig. 2 |. Purification of SMYD5 catalytic activity in cell lysates to identify UBA52 as candidate substrate.

a, Western blots of WCEs from control or SMYD5-depleted KKLS and U2OS cells used in **b** as substrates. **b**, SMYD5 methylates a ~ 10 kDa protein in KKLS and U2OS cell lysates. In vitro methylation assays as in Fig. 1d with the indicated enzymes and WCEs in **a** as substrates. **c**, The candidate SMYD5 substrate migrates faster than histone H4. In vitro methylation reactions as in **b** with the indicated KMT enzymes or GST alone as a negative control using SMYD5-depleted A549 WCEs as substrates as in Fig. 1d. Red arrowhead, SMYD5-dependent methylated protein. Blue arrowhead, SETD8-dependent histone H4 methylated at K20. **d**, Substantial enrichment of SMYD5-dependent methylated protein in extracts at 4th fractionation step (see schematic Fig. 1e). In vitro methylation assays as in Fig. 1d with the indicated enzymes using as substrate SMYD5-depleted A549 WCE, Input (lysate after 3 fractionation steps: (1) cytoplasmic isolation, (2) ammonium sulfate salt precipitation, and (3) hydrophobic interaction chromatography), and the indicated fractions

(1–13) of the input material separated by size-exclusion chromatography. The Coomassie staining demonstrates the enrichment of the activity relative to total proteins present in the starting material. The region around the ~10 kDa band signal in Fraction 13, which showed the highest degree of purification, was analyzed by mass spectrometry (See Supplementary Tables 1–4). **e**, 2D gel electrophoresis separation of Fraction 13 in **d** further purifies the SMYD5-dependent methylated ~10kD protein. Red asterisk, SMYD5-dependent methyl band. The region around the red asterisk was analyzed by mass spectrometry to obtain UBA52 as the top hit. Left: Silver stain of 2D separation of Fraction 13 proteins; Middle: ^{3}H-SAM was used as methyl donor and the methylation was visualized by autoradiography. Right: merge of the two panels.

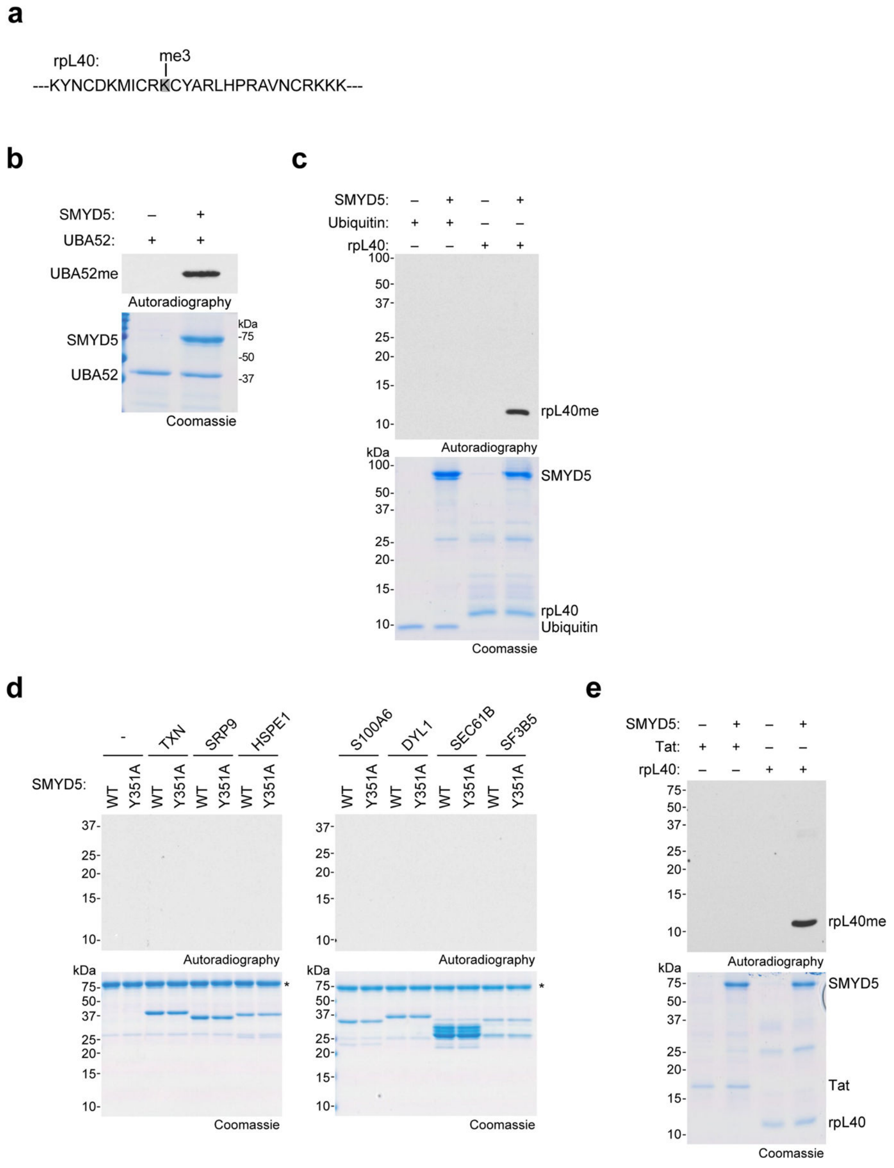

Extended Data Fig. 3 |. SMYD5 specifically methylates rpL40 and has no activity on many other putative substrates in vitro.

a, The sequence of human rpL40 protein surrounding lysine 22. The site of methylation at K22 is indicated. Due to the many charged residues and the specific residues surrounding K22, irrespective of proteases, it is challenging to obtain suitable peptides for MS-based identification. **b**, SMYD5 methylates recombinant un-cleaved UBA52 protein in vitro. c, SMYD5 methylates recombinant rpL40 but not ubiquitin alone. **d**, Besides UBA52, SMYD5 did not in vitro methylate several other candidate proteins identified as potential candidates by MS/MS analysis of fraction 13 described in Extended Data Fig. 2d. **e**, SMYD5 does not in vitro methylate HIV-1 Tat protein. rpL40 is shown as a positive control.

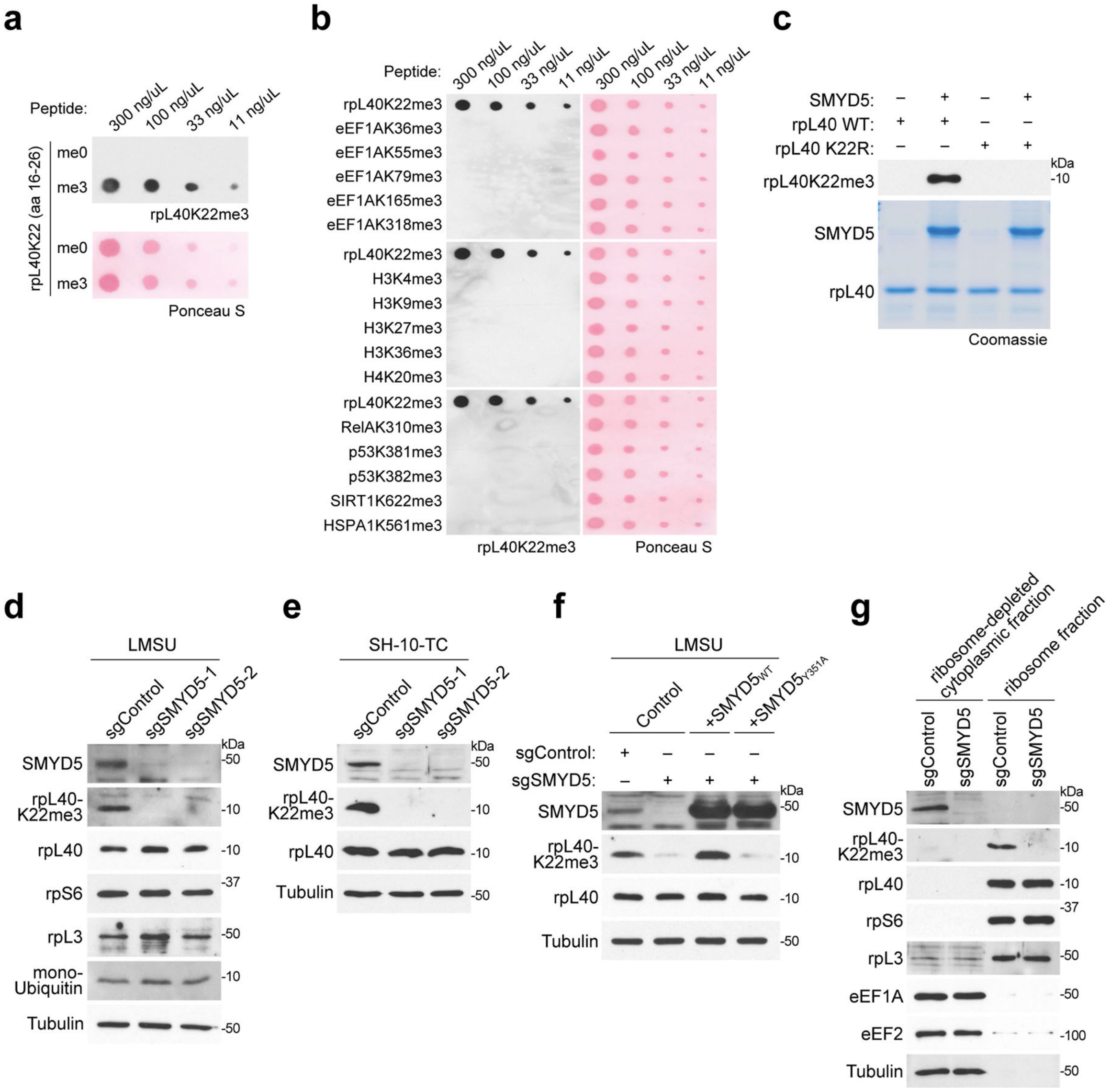

Extended Data Fig. 4 |. Generation of a specific rpL40K22me3 antibody and evidence that SMYD5 is the principal enzyme that physiologically generates rpL40K22me3.

a, rpL40K22me3 antibody recognizes cognate methylated peptide sequence but not unmethylated peptide. Dot blot analysis with the indicated rpL40 peptides spanning amino acids (16–26) at the indicated concentrations probed with the rpL40K22me3 antibody (top) or stained with Ponceau S (bottom) to control for loading. **b**, rpL40K22me3 antibody recognizes cognate methylated peptide sequence but does not recognize several other histone and non-histone peptides harboring trimethylation. Dot bot analysis as in **a**. **c**, Western blot with the rpL40K22me3 antibody of in vitro methylation reactions with the indicated enzyme and substrates. **d**-**e**, Western blots with the indicated antibodies of WCEs from **d**, LMSU and **e**, SH-10-TC cell lines expressing CRISPR-Cas9 and two independent sgRNAs targeting *SMYD5* or a control sgRNA. Tubulin was used as loading control. **f**, Western blots of SMYD5-depleted LMSU cells complemented with CRISPR-resistant SMYD5$_{WT}$, SMYD5$_{Y351A}$ catalytic mutant, or control plasmid. **g**, Western blots with indicated antibodies of sucrose-cushion purified ribosome-depleted cytoplasmic lysates and ribosomes-enriched fractions from KKLS cells.

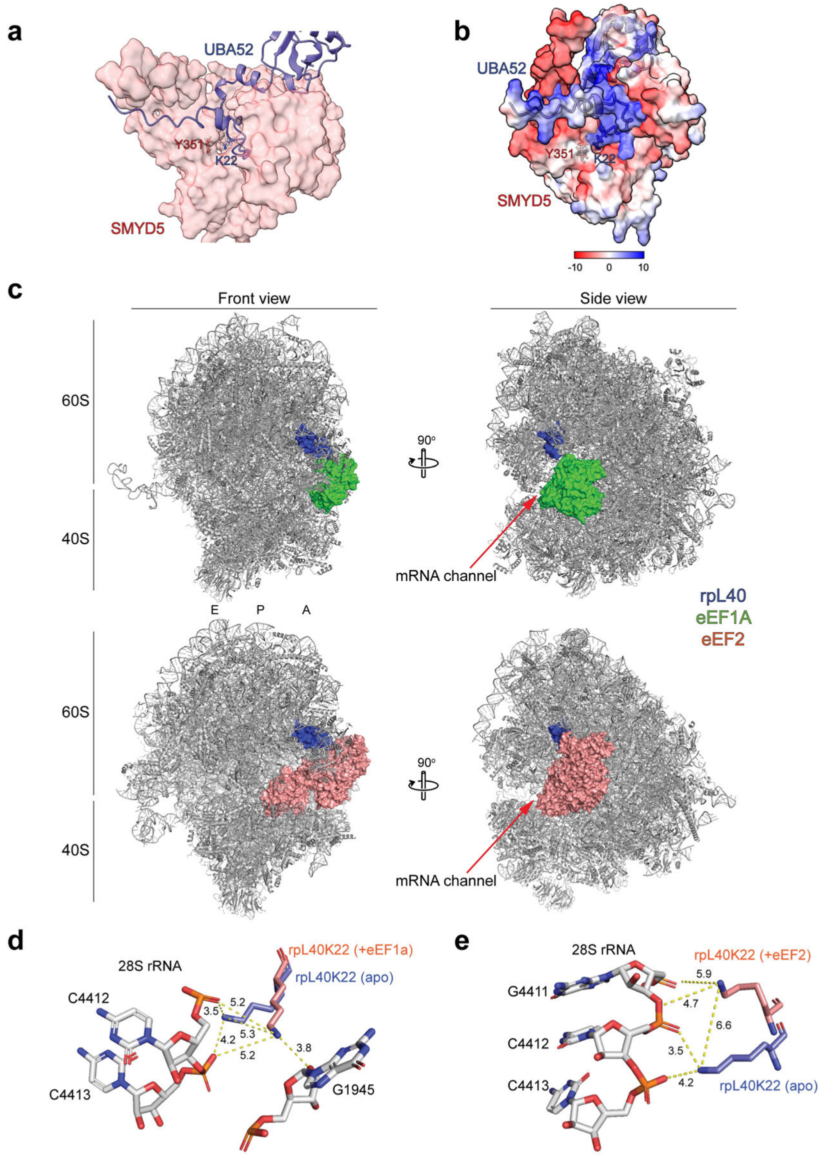

Extended Data Fig. 5 |. Alphafold analysis of SMYD5-rpL40 interaction and structural analysis of rpL40 in human ribosomes.

a-**b**, UBA52 + SMYD5 predicted structures (AlphaFold v2.3; see Methods) **a**, UBA52/ rpL40 depicted by blue cartoon and SMYD5 by red molecular surface, as indicated. K22 of rpL40 the SMYD5 catalytic tunnel-forming residue (Y351) are shown. K22 of rpL40 directly inserts into SMYD5's catalytic tunnel. **b**, UBA52 + SMYD5 predicted structures coloured by electrostatic charge. Colouring key depicts predict Coulombic electrostatic potential, with red corresponding to negative charge and blue corresponding to positive charge. rpL40 substrate lysine K22 and SMYD5 catalytic Y351 are shown. **c**-**e**, Ribosome-bound rpL40 undergoes rearrangements through different stages of elongation factor association. **c**, Top, ribbon representation of the overall complex of human 80 S ribosomes bound to eEF1A (PDB: 6ZMO), bottom, human 80 S ribosomes bound to eEF2 (PDB: 6D9J). rpL40, eEF1A and eEF2 are shown in surface representations and differentially coloured as indicated. **d**-**e**, close-up view of potential intermolecular interaction between rpL40K22 and adjacent 28 S rRNA. Distances are provided of hydrogen-bonding interactions depicted as dashed lines. **d**, rpL40K22 (shown in blue) from apo human 80 S ribosome structure (PDB: 4UG0) that is not bound to initiation/elongation factors and has close interactions with the 28 S rRNA at bases C4412 and C4413. rpL40K22 (shown in red) from 80 S ribosome bound to eEF1a (PDB: 6ZMO) leads to a shift in K22 of 5.3 Å toward an ionic interaction with G1945 of the 28 S rRNA. **e**, as in **d** but replacing eEF1A with 80 S ribosome bound to eEF2 (PDB: 6D9J), rpL40K22 shifts by 6.6 Å in favor of more distant interactions with G4411.

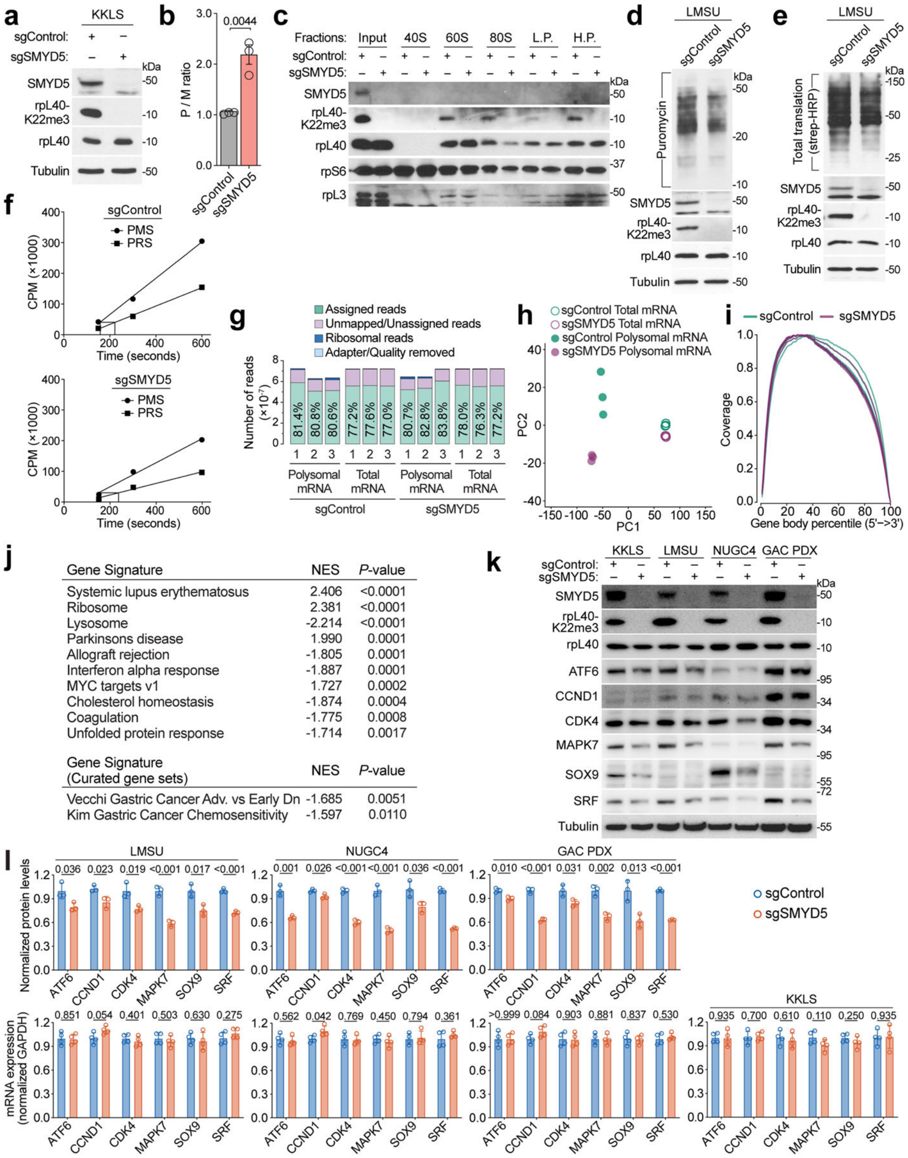

Gene Signature	NES	*P*-value
Systemic lupus erythematosus	2.406	<0.0001
Ribosome	2.381	<0.0001
Lysosome	-2.214	<0.0001
Parkinsons disease	1.990	0.0001
Allograft rejection	-1.805	0.0001
Interferon alpha response	-1.887	0.0001
MYC targets v1	1.727	0.0002
Cholesterol homeostasis	-1.874	0.0004
Coagulation	-1.775	0.0008
Unfolded protein response	-1.714	0.0017

Gene Signature (Curated gene sets)	NES	*P*-value
Vecchi Gastric Cancer Adv. vs Early Dn	-1.685	0.0051
Kim Gastric Cancer Chemosensitivity	-1.597	0.0110

Extended Data Fig. 6 |. SMYD5 regulates ribosome dynamics and mRNA translation programs.

a, Western blots with the indicated antibodies of WCEs from the KKLS cells used in Fig. 2b. **b**, Ratio of area under polysomes (P) and monosome (M) peaks as in Fig. 2c from polysome profiling experiments of control or SMYD5-depleted LMSU cells fractionated on 10%–50% sucrose gradients are calculated and presented as P/M ratio from three independent biological replicates. *P*-value was determined by two-tailed unpaired t-test. **c**, Western analysis with the indicated antibodies of the indicated fractions from the polysome profiling experiments in KKLS cells as in Fig. 2b. **d-e**, SMYD5 depletion in LMSU cells leads to reduced global protein synthesis. **d**, Puromycylation assays in control or SMYD5-depleted LMSU cells. WCEs were probed with the indicated antibodies. **e**, AHA labeling assays as in (d). WCEs were probed with the indicated antibodies or HRP-strepavidin was used to detect biotin-clicked AHA. **f**, Linear regression analysis of ribosome half-transit time in control or SMYD5-depleted KKLS cells. PMS, post-mitochondrial supernatants (complete

+ nascent proteins); PRS, post-ribosomal supernatant (complete proteins). A representative graph is shown from four independent biological replicates. **g**, Summary of sequencing reads distribution mapped to the indicated categories. **h**, Principal component analysis (PCA) of the indicates datasets. **i**, Quality assessment of reads distribution across gene bodies, the absence of 3’ and 5’ bias indicates absence of high levels of RNA degradation (see Methods for **g**-**i**). **j**, GSEA analysis identifies the top significantly enriched signatures (Hallmark, KEGG, and selected) in differential polysome-associated mRNAs from Control versus SMYD5-depleted KKLS cells data sets (n = 3 biologically independent samples per group). Normalized enrichment scores (NES) and nominal *P*-values are shown. **k**, Westerns of the indicated proteins in control or SMYD5-depleted cell lines or GAC PDX samples as indicated (for KKLS, Western is representative of data from Fig. 2j). **l**, Quantification of Western signal (top row) and mRNA by RT-PCR (bottom row) for the indicated genes in the indicated cell lines ±SMYD5 as indicated. Data are represented as mean ± s.e.m. of three independent biological replicates.

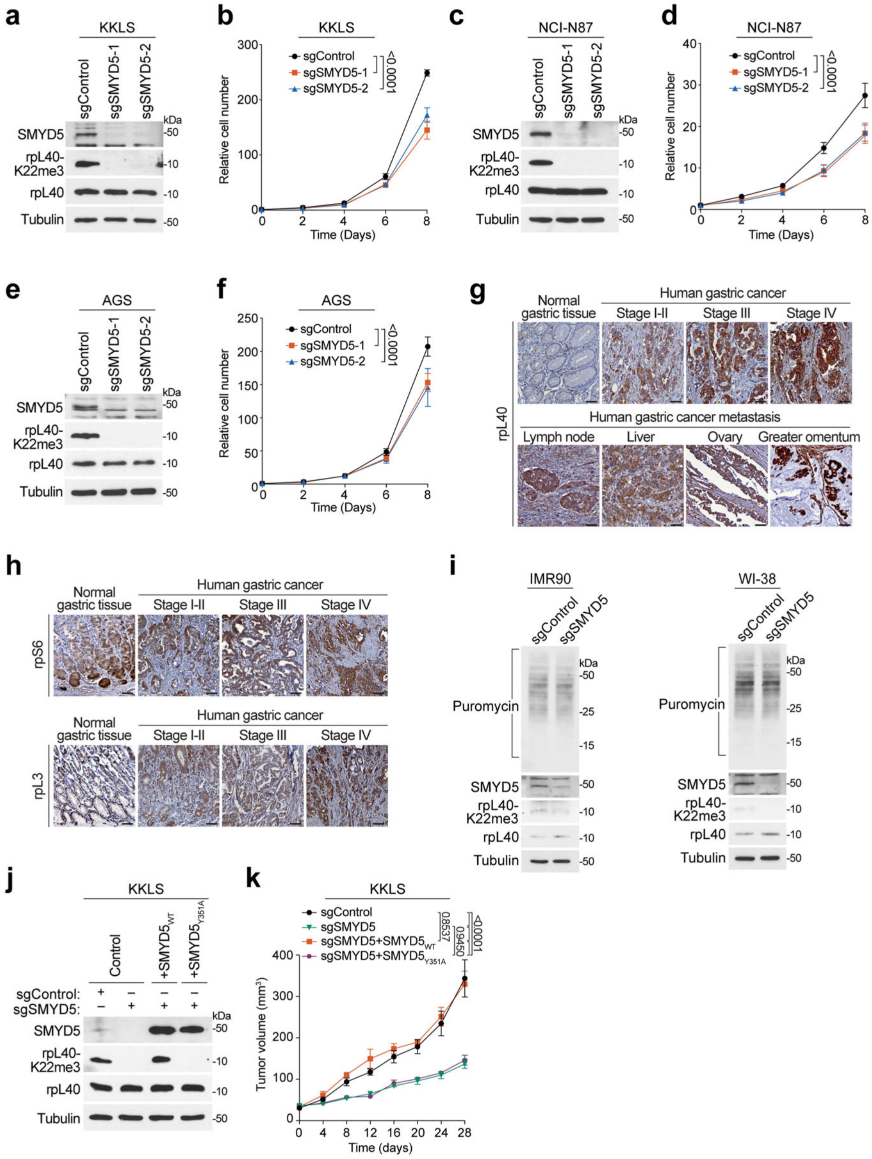

Extended Data Fig. 7 |. SMYD5 and rpL40 K22me3 promote cancer cell proliferation.

a-**f**, SMYD5 depletion inhibits proliferation of KKLS (**a**,**b**), NCI-N87 (**c**,**d**) and AGS (**e**,**f**) cells. **a**, **c**, **e**, Western blots with the indicated antibodies of the indicated WCEs expressing CRISPR-Cas9 and two independent sgRNAs targeting *SMYD5* or a control sgRNA. **b**, **d**, **f**, proliferation of cells shown in **a**, **c**, **e**, respectively. Data are represented as mean ± s.e.m from three biologically independent experiments. *P*-values were determined by two-tailed unpaired t-test. **g**, Representative immunohistochemical staining with rpL40 antibody of patient samples from normal gastric tissue (n = 12), GAC at advancing stages (n = 48 (stage I/II), 72 (III) and 16 (IV)) and GAC metastasis at the indicated organs (n = 34), scale bars: 100 μm. **h**, Representative immunohistochemical staining with rpS6 and rpL3 antibody of patient samples from normal gastric tissue (n = 12) and GAC at advancing stages (n = 48 (stage I/II), 72 (III) and 16 (IV)), scale bars: 100 μm. **i**, Puromycylation assays in control or SMYD5-depleted WI-38 (left), IMR-90 (right) cells. WCEs were probed with the indicated antibodies. **j**, Western blot analysis with the indicated antibodies of lysates from SMYD5-depleted KKLS gastric cancer cells complemented with CRISPR-resistant $SMYD5_{WT}$ or $SMYD5_{Y351A}$. **k**, Tumor volume quantification for KKLS xenografts modified to express sgRNA SMYD5 or sgRNA control and overexpressing CRISPR-resistant $SMYD5_{WT}$ or catalytically deficient $SMYD5_{Y351A}$ as indicated (see **j** for Western blot analyses) in NSG mice (n = 5 mice, for each treatment group). *P*-values were calculated by two-way ANOVA with Tukey testing for multiple comparisons. Data are represented as mean ± s.e.m.

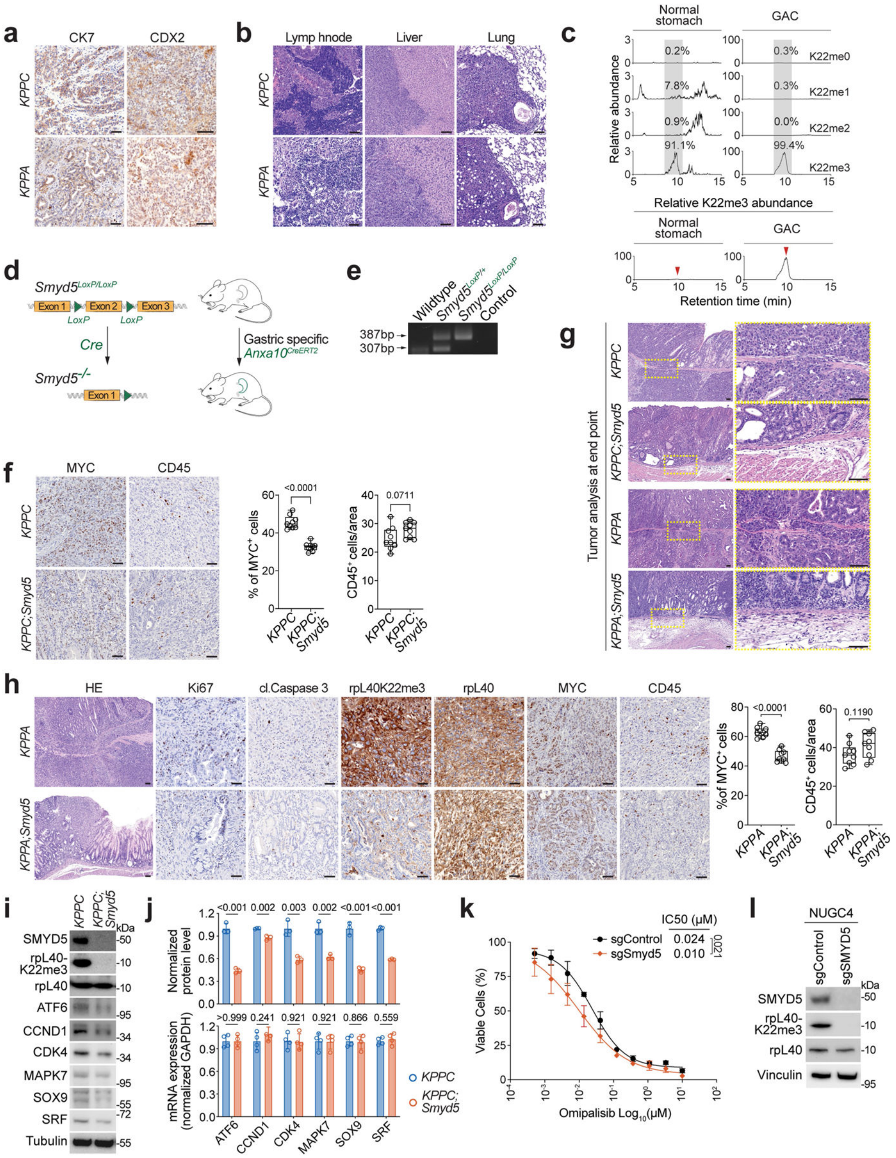

Extended Data Fig. 8 |. SMYD5 deletion represses malignant GAC tumorigenesis in vivo.

a, Representative IHC staining of gastric tumors from *KPPC* and *KPPA* models exhibit key histological features of human GAC, including positive staining for cytokeratin 7 (CK7) and CDX2 (representative of n = 9 samples for each group). Scale bars, 100 μm. **b**, Representative HE-stained section of gastric cancer lymph node, liver, and lung metastasis observed in *KPPC* and *KPPA* models. Scale bars, 100 μm. **c**, Schematic of the *Smyd5*$^{LoxP/LoxP}$ conditional allele. In the presence of Cre recombinase, exon 2 is deleted to disrupt *Smyd5* expression. **d**, Confirmation of *Smyd5*$^{LoxP/LoxP}$ conditional allele by PCR on DNA isolated from mouse tailbiopsies from indicated mouse genotypes, expected product sizes are marked. **e**, Left: Selected ion chromatograms for non-, mono-, di- and tri-methyl rpL40K22 peptides from Chymotrypsin digestion of endogenous rpL40 immunoprecipitated from biopsies from normal stomach tissue and GAC *KPPC* tissue. Note the Y axis scales for relative abundance are different between normal and tumor samples (see right panel for comparison of abundance of rpL40K22me3 peptides between normal and tumor samples). HPLC elution profiles show a 10-ppm mass window around expected peptide masses (peptide sequence ICR$\underline{\text{K}}$CY, K22 is underlined; *m/z* are 300.4791, 305.1509, 309.8228, and 314.4947). Right: ion chromatograms for trimethyl rpL40K22 peptides as in the left panel using the Y axis scale from the tumor sample. Arrow indicates the relevant peak as in the left panel. **f**, Representative immunohistochemical staining and quantification of MYC and CD45 positive cells in gastric tumors from *KPPC* and *KPPC;Smyd5* mutant mice at 6 weeks after tamoxifen induction (representative of n = 9 mice for each experimental group). Scale bars 100 μm. **g**, Representative HE-stained sections of gastric cancers at endpoint (severe morbidity) from *KPPC* and *KPPA* models indicate malignant histopathology with notable cancer cell invasion through basement membrane (dash line area with magnification). Scale bars 100 μm. **h**, Representative HE-stained sections, immunohistochemical staining with indicated antibodies and quantification of MYC and CD45 positive cells in gastric tumors from *KPPA* and *KPPA;Smyd5* mutant mice at 6 weeks after tamoxifen induction (representative of n = 9 mice for each experimental group). Scale bars 100 μm. **i**, Westerns of the indicated proteins in tissue biopsy lysates from *KPPC* and *KPPC;Smyd5* mutant mice. **j**, Quantification of Western signal (top) and mRNA by RT-PCR (bottom) for the indicated genes in tissue biopsy lysates from *KPPC* and *KPPC;Smyd5* mutant mice. Data are represented as mean ± s.e.m. of three (Western) or four (RT-PCR) independent replicates. **k**, Dose-response analysis and half maximal inhibitory concentration values (IC50) for Omipalisib in LMSU GAC cell line ±SMYD5 knockdown. Data are represented as mean ± s.e.m. from three independent biological replicates. **l**, Western blot analysis with the indicated antibodies of WCE of control and SMYD5-depleted NUGC4 gastric cancer cell line. Boxes: 25th to 75th percentile, whiskers: min. to max., center line: median.

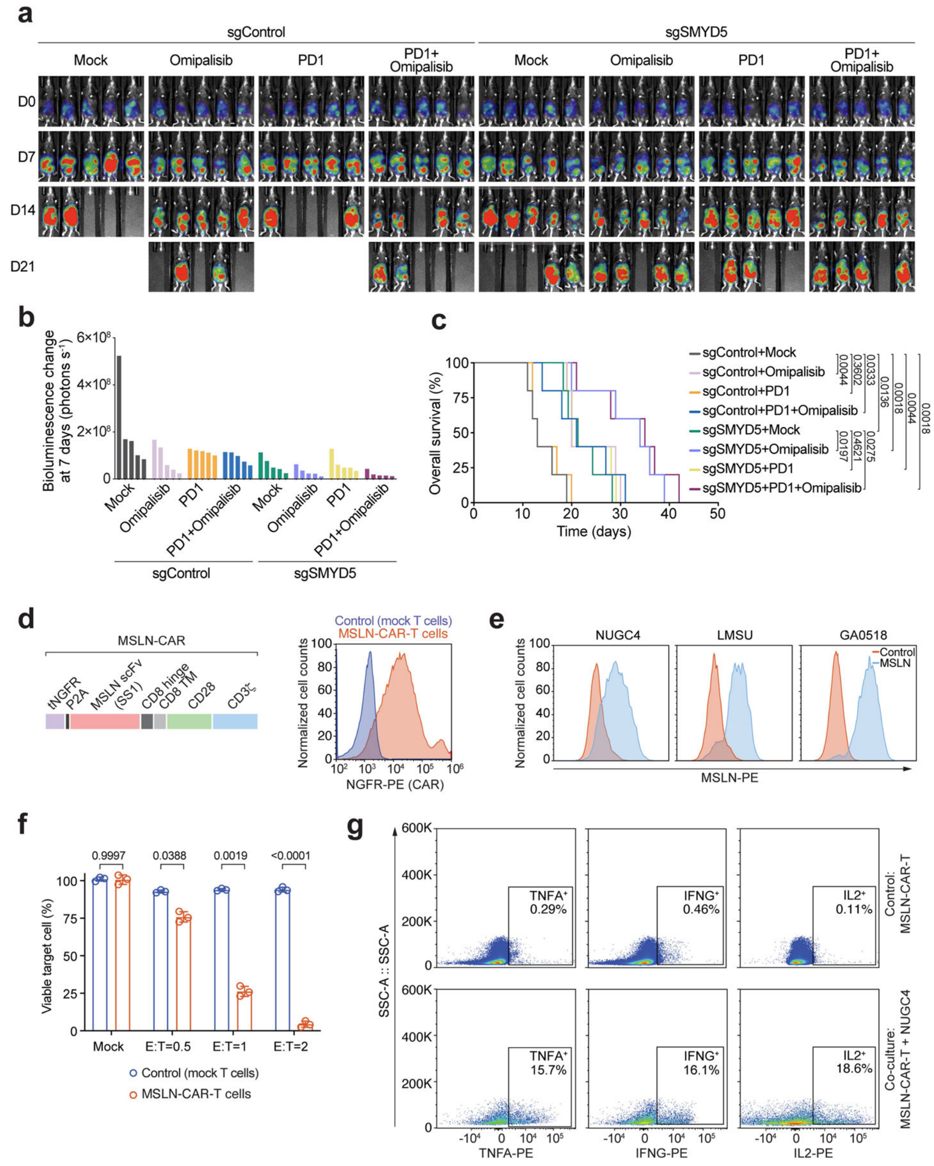

Extended Data Fig. 9 |. Analysis of therapeutic efficacy of PD1 and Mesothelin (MSLN)-CAR T cells immunotherapies against gastric cancer cells.

a, Representative bioluminescence imaging of syngeneic peritoneal carcinomatosis allograft model established in syngeneic mice from *KPPC* peritoneal metastases cells ±SMYD5 to test the efficacy of PD1 therapy. Animals were treated with ±PD1 (10 mg/kg, twice per week) and ±Omipalisib (4 mg/kg, daily) and tumor growth was monitored by bioluminescence imaging (n = 5 mice per group). **b**, Waterfall plot of *KPPC* ± SMYD5 allograph bioluminescence signal changes in individual mice receiving the indicated therapies (n = 5 mice per group). **c**, Kaplan-Meier survival curves of *KPPC* ± SMYD5 allograph receiving the indicated treatments. *P*-values were determined by log-rank test for significance. n = 5 mice per group. **d**, MSLN-CAR expression vector design containing truncated human nerve growth factor receptor (tNGFR), self-cleaving P2A peptide sequence followed by MSLN-specific scFv (SS1), the CD8a hinge, transmembrane, and CD28-CD3ζ co-stimulatory domain. tNGFR serves as a cell surface reporter to enable specific detection of CAR-expressing cells by flow cytometry. The right panel shows a representative flow cytometry plot identifying MSLN-CAR expressing T cells using NGFR staining. **e**, MSLN is a cell-surface glycoprotein expressed in NUGC4, LMSU cell lines and GAC-PDX cells as detected by flow cytometry. **f**, MSLN-CAR T cells co-cultured with MSLN$^+$ NUGC4 cells shows selective killing of MSLN$^+$ target cancer cells. Data are represented as mean ± s.e.m. from three independent biological replicates. **g**, MSLN-CAR T cells co-cultured with MSLN$^+$ NUGC4 target cancer cells and analyzed for intracellular IL−2, IFN-γ and TNF-α cytokine levels by flow cytometry indicative of CAR T cell activation by MSLN$^+$ target cells stimulation. Representative of three independent experiments is shown.

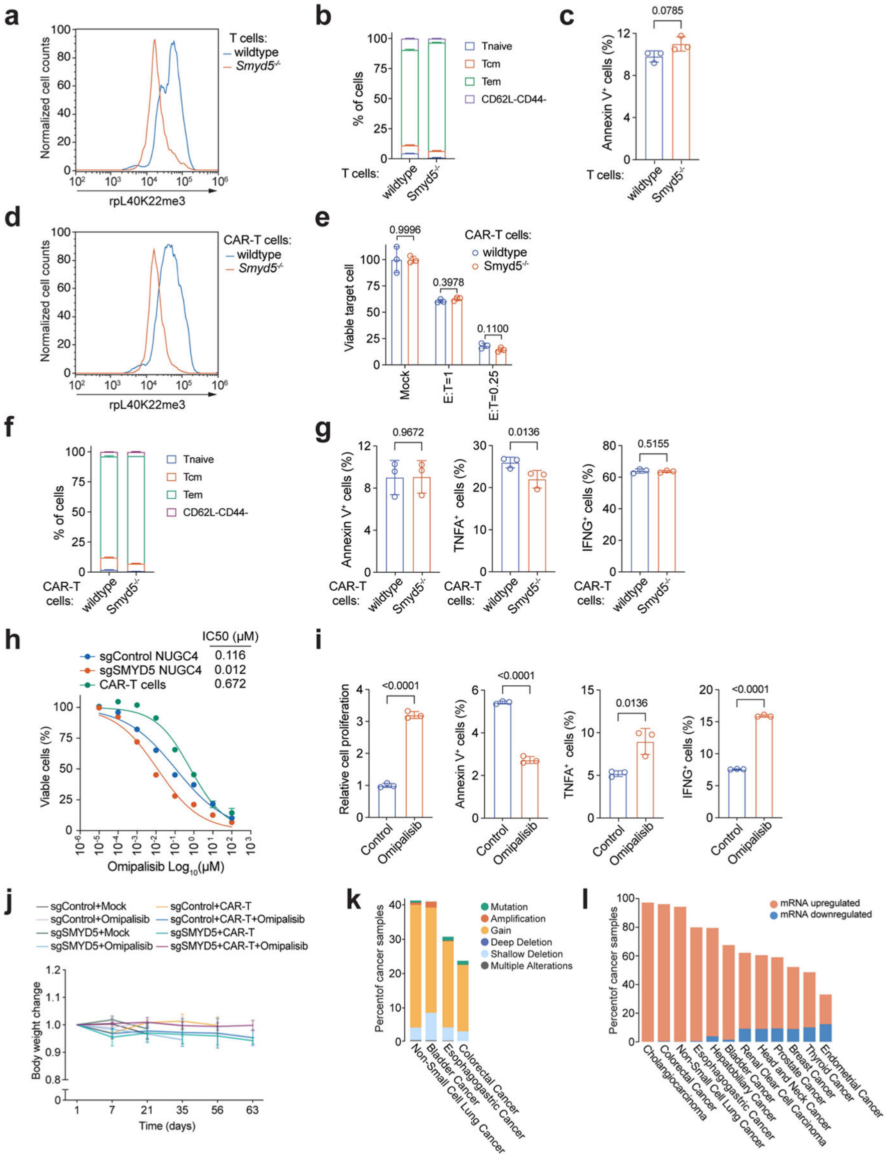

Extended Data Fig. 10 |. SMYD5 ablation or treatment with Omipalisib does not negatively impact CAR T cells efficacy and *SMYD5* genetic alterations and mRNA expression in diverse cancers.

a, T cells isolated from *Smyd5*$^{LoxP/LoxP}$ conditional knockout were transduced with retrovirus expressing Cre- recombinase (*Smyd5*$^{-/-}$) or mock control (wildtype). SMYD5 depletion was validated with rpL40 K22me3 specific antibody by flow cytometry. Representative of three independent experiments. **b**, Wildtype and *Smyd5* deleted T cells exhibit similar distribution of naive (T_{naive}; CD62L$^+$CD44$^-$), central memory (T_{cm}; CD62L$^+$CD44$^+$), effector memory (T_{em}; CD62L$^-$CD44$^+$) and CD62L$^-$CD44$^-$ cell subsets. Data are represented as mean ± s.e.m. from three independent biological replicates. **c**, SMYD5 ablation in T cells does not significantly change the rate of apoptosis as assessed by Annexin V flow cytometry analysis. Data are represented as mean ± s.e.m. from three independent biological replicates. *P*-values were determined by a two-tailed unpaired t-test. **d**, MSLN-CAR T cells were generated from *Smyd5*$^{LoxP/LoxP}$ conditional knockout by transduction with retrovirus expressing CAR and Cre- recombinase (CAR T *Smyd5*$^{-/-}$) or CAR only control (CAR T wildtype). SMYD5 depletion was validated with rpL40K22me3 specific antibody by flow cytometry. Representative of three independent experiments. **e**, Depletion of SMYD5 deletion does not inhibit MSLN-CAR T cells cytotoxicity against MSLN$^+$ NUGC4 gastric cancer target cells. Data are represented as mean ± s.e.m. from three independent biological replicates. *P*-values were determined by a two-tailed unpaired t-test. **f**, Wildtype and *Smyd5* deleted MSLN-CAR T cells exhibit similar distribution of naive (T_{naive}; CD62L$^+$CD44$^-$), central memory (T_{cm}; CD62L$^+$CD44$^+$), effector memory (T_{em}; CD62L$^-$CD44$^+$) and CD62L$^-$CD44$^-$ cell subsets. Data are represented as mean ± s.e.m. from three independent biological replicates. **g**, Depletion of SMYD5 does not significantly impact MSLN-CAR T cells apoptosis (Annexin V staining) or intracellular IFN-γ and TNF-α cytokine levels analyzed by flow cytometry following co-culture with MSLN$^+$ NUGC4 target cells for 6 h. Data are represented as mean ± s.e.m. from three independent biological replicates. *P*-values were determined by a two-tailed unpaired t-test. **h**, Dose-response analysis and half maximal inhibitory concentration values (IC50) for Omipalisib in NUGC4 cells and CAR T cells shows that Omipalisib treatment more strongly suppresses SMYD5-depleted vs. control NUGC4 viability and has a much weaker impact on MSLN-CAR T cell viability at concentrations that effectively impact NUGC4 viability. Data from three independent biological replicates. **i**, Omipalisib treatment does not negatively impact MSLN-CAR T cell functions. CAR T cells were treated with Omipalisib at a concentration of 0.1 μM for 8 h, followed by co-culture with MSLN$^+$ NUGC4 gastric cancer target cells for 6 h. Cell proliferation (cytoblue), apoptosis (Annexin V) and intracellular IFN-γ and TNF-α cytokine levels were analyzed by flow cytometry. Data are represented as mean ± s.e.m. from three independent biological replicates. *P*-values were determined by a two-tailed unpaired t-test. **j**, NUGC4 PC xenografted animal weight measurements over the course of the indicated treatments up to 63 days (as in Figs. 5e–g and i–l). Data are represented as mean ± s.e.m. of n = 5 mice per group. **k**, Copy number gain is the most frequent genetic alternation of *SMYD5* present in common tumor types (TCGA data). **l**, *SMYD5* expression relative to normal samples is elevated across diverse cancer types (TCGA data).

Supplementary Material

Refer to Web version on PubMed Central for supplementary material.

Acknowledgements

We thank members of the Gozani and Mazur laboratories for critical reading of the manuscript; M. Ott for providing *Tat1* cDNA and M. Oeffinger and C. Trahan for ribosome biogenesis protocols. This work was supported in part by grants from the NIH to O.G. (R35 GM139569), O.G. and P.K.M. (R01 CA236118, R01 CA278940 and R01 CA272844), P.K.M. (R01 CA236949, R01 CA266280 and R01 CA272843), B.A.G. (R01 HD106051 and R01 AI118891), J.W.F. and J.J. (5T32GM007276), J.W.F. (F31CA261128), and P.J. by an FRQS Doctoral award. P.K.M. is also supported by a DoD PRCRP Career Development Award (CA181486), CPRIT IIRA (RP220391) and CPRIT Scholar in Cancer Research (RR160078). B.A.G is also supported by NSF CHE-2127882. N.M.F. is supported by the American Cancer Society postdoctoral fellowship. I.T. is a Senior Scholar of the Fonds de la recherche du Québec–Santé (FRQS) and is in part supported by a grant from the Canadian Institutes of Health Research (CIHR PJT-175050). O.L. is supported by the Swedish Research Council (2020–01665), the Swedish Cancer Society (22 2186), the Stockholm Cancer Society (211222) and the Wallenberg Academy Fellow programme. J.P. received support from the Korean Government Scholarship Program for Study Abroad (NIIED).

Data availability

Plasmids, antibodies and cell lines generated in this study will be available from the lead contact upon request with a completed material transfer agreement. The RNA sequencing data for total mRNA and polysome-associated mRNA have been deposited into the Gene Expression Omnibus database under accession number GSE238257. MS data have been deposited into the ProteomeXchange Consortium through the PRIDE partner repository with the dataset identifiers PXD052358 and PXD052359. Source data are provided with this paper.

References

1. Robichaud N, Sonenberg N, Ruggero D & Schneider RJ Translational control in cancer. Cold Spring Harb. Perspect. Biol 11, a032896 (2019). [PubMed: 29959193]
2. Kovalski JR, Kuzuoglu-Ozturk D & Ruggero D Protein synthesis control in cancer: selectivity and therapeutic targeting. EMBO J 41, e109823 (2022). [PubMed: 35315941]
3. Baker RT & Board PG The human ubiquitin-52 amino acid fusion protein gene shares several structural features with mammalian ribosomal protein genes. Nucleic Acids Res 19, 1035–1040 (1991). [PubMed: 1850507]
4. Morgan E et al. The current and future incidence and mortality of gastric cancer in 185 countries, 2020–40: a population-based modelling study. eClinicalMedicine 47, 101404 (2022). [PubMed: 35497064]
5. Hirata Y, Noorani A, Song S, Wang L & Ajani JA Early stage gastric adenocarcinoma: clinical and molecular landscapes. Nat. Rev. Clin. Oncol 20, 453–469 (2023). [PubMed: 37264184]
6. Manzanedo I, Pereira F, Perez-Viejo E & Serrano A Gastric cancer with peritoneal metastases: current status and prospects for treatment. Cancers 15, 1777 (2023). [PubMed: 36980663]
7. Bhat KP, Umit Kaniskan H, Jin J & Gozani O Epigenetics and beyond: targeting writers of protein lysine methylation to treat disease. Nat. Rev. Drug. Discov 20, 265–286 (2021). [PubMed: 33469207]
8. Meng X et al. Comprehensive analysis of histone modification-associated genes on differential gene expression and prognosis in gastric cancer. Exp. Ther. Med 18, 2219–2230 (2019). [PubMed: 31452712]
9. Zhang Y et al. Unique SMYD5 structure revealed by AlphaFold correlates with its functional divergence. Biomolecules 12, 783 (2022). [PubMed: 35740908]
10. Zhang Y et al. SMYD5 catalyzes histone H3 lysine 36 trimethylation at promoters. Nat. Commun 13, 3190 (2022). [PubMed: 35680905]
11. Stender JD et al. Control of proinflammatory gene programs by regulated trimethylation and demethylation of histone H4K20. Mol. Cell 48, 28–38 (2012). [PubMed: 22921934]

12. Husmann D & Gozani O Histone lysine methyltransferases in biology and disease. Nat. Struct. Mol. Biol 26, 880–889 (2019). [PubMed: 31582846]

13. Afjehi-Sadat L & Garcia BA Comprehending dynamic protein methylation with mass spectrometry. Curr. Opin. Chem. Biol 17, 12–19 (2013). [PubMed: 23333572]

14. Stark C et al. BioGRID: a general repository for interaction datasets. Nucleic Acids Res 34, D535–D539 (2006). [PubMed: 16381927]

15. Williamson NA, Raliegh J, Morrice NA & Wettenhall RE Post-translational processing of rat ribosomal proteins. Ubiquitous methylation of Lys22 within the zinc-finger motif of RL40 (carboxy-terminal extension protein 52) and tissue-specific methylation of Lys4 in RL29. Eur. J. Biochem 246, 786–793 (1997). [PubMed: 9219540]

16. Jumper J et al. Highly accurate protein structure prediction with AlphaFold. Nature 596, 583–589 (2021). [PubMed: 34265844]

17. Eastham MJ, Pelava A, Wells GR, Watkins NJ & Schneider C RPS27a and RPL40, which are produced as ubiquitin fusion proteins, are not essential for p53 signalling. Biomolecules 13, 898 (2023). [PubMed: 37371478]

18. Shi Z et al. Heterogeneous ribosomes preferentially translate distinct subpools of mRNAs genome-wide. Mol. Cell 67, 71–83.e7 (2017). [PubMed: 28625553]

19. Guimaraes JC & Zavolan M Patterns of ribosomal protein expression specify normal: and malignant human cells. Genome Biol 17, 236 (2016). [PubMed: 27884178]

20. Ferretti MB & Karbstein K Does functional specialization of ribosomes really exist? RNA 25, 521–538 (2019). [PubMed: 30733326]

21. Miller SC, MacDonald CC, Kellogg MK, Karamysheva ZN & Karamyshev AL Specialized ribosomes in health and disease. Int. J. Mol. Sci 24, 6334 (2023). [PubMed: 37047306]

22. Panda A et al. Tissue- and development-stage-specific mRNA and heterogeneous CNV signatures of human ribosomal proteins in normal and cancer samples. Nucleic Acids Res 48, 7079–7098 (2020). [PubMed: 32525984]

23. Lee AS, Burdeinick-Kerr R & Whelan SP A ribosome-specialized translation initiation pathway is required for cap-dependent translation of vesicular stomatitis virus mRNAs. Proc. Natl Acad. Sci. USA 110, 324–329 (2013). [PubMed: 23169626]

24. Gandin V et al. Polysome fractionation and analysis of mammalian translatomes on a genome-wide scale. J. Vis. Exp 87, 51455 (2014).

25. Liu S et al. METTL13 methylation of eEF1A increases translational output to promote tumorigenesis. Cell 176, 491–504.e421 (2019). [PubMed: 30612740]

26. Schmidt EK, Clavarino G, Ceppi M & Pierre P SUnSET, a nonradioactive method to monitor protein synthesis. Nat. Methods 6, 275–277 (2009). [PubMed: 19305406]

27. Iwasaki S & Ingolia NT The growing toolbox for protein synthesis studies. Trends Biochem. Sci 42, 612–624 (2017). [PubMed: 28566214]

28. Nielsen PJ & McConkey EH Evidence for control of protein synthesis in HeLa cells via: the elongation rate. J. Cell. Physiol 104, 269–281 (1980). [PubMed: 7419605]

29. Oertlin C et al. Generally applicable transcriptome-wide analysis of translation using anota2seq. Nucleic Acids Res 47, e70 (2019). [PubMed: 30926999]

30. Oertlin C, Watt K, Ristau J & Larsson O Anota2seq analysis for transcriptome-wide atudies of mRNA translation. Methods Mol. Biol 2418, 243–268 (2022). [PubMed: 35119670]

31. Truitt ML & Ruggero D New frontiers in translational control of the cancer genome. Nat. Rev. Cancer 16, 288–304 (2016). [PubMed: 27112207]

32. Lim HJ, Zhuang L & Fitzgerald RC Current advances in understanding the molecular profile of hereditary diffuse gastric cancer and its clinical implications. J. Exp. Clin. Cancer Res 42, 57 (2023). [PubMed: 36869400]

33. Gregory SN & Davis JL CDH1 and hereditary diffuse gastric cancer: a narrative review. Chin. Clin. Oncol 12, 25 (2023). [PubMed: 37303221]

34. Pihlak R, Fong C & Starling N Targeted therapies and developing precision medicine in gastric cancer. Cancers 15, 3248 (2023). [PubMed: 37370858]

35. Seidlitz T et al. Mouse models of human gastric cancer subtypes with stomach-specific CreERT2-mediated pathway alterations. Gastroenterology 157, 1599–1614.e2 (2019). [PubMed: 31585123]
36. Wong HH & Chu P Immunohistochemical features of the gastrointestinal tract tumors. J. Gastrointest. Oncol 3, 262–284 (2012). [PubMed: 22943017]
37. Zhao L et al. Paracrine activation of MET promotes peritoneal carcinomatosis in scirrhous gastric cancer. Cancer Sci 104, 1640–1646 (2013). [PubMed: 24118504]
38. Staudt RE, Carlson RD & Snook AE Targeting gastrointestinal cancers with chimeric antigen receptor (CAR)-T cell therapy. Cancer Biol. Ther 23, 127–133 (2022). [PubMed: 35129050]
39. Sadelain M, Riviere I & Riddell S Therapeutic T cell engineering. Nature 545, 423–431 (2017). [PubMed: 28541315]
40. Labanieh L & Mackall CL CAR immune cells: design principles, resistance and the next generation. Nature 614, 635–648 (2023). [PubMed: 36813894]
41. Qi C et al. Claudin18.2-specific CAR T cells in gastrointestinal cancers: phase 1 trial interim results. Nat. Med 28, 1189–1198 (2022). [PubMed: 35534566]
42. Carpenito C et al. Control of large, established tumor xenografts with genetically retargeted human T cells containing CD28 and CD137 domains. Proc. Natl Acad. Sci. USA 106, 3360–3365 (2009). [PubMed: 19211796]
43. Lv J et al. Mesothelin is a target of chimeric antigen receptor T cells for treating gastric cancer. J. Hematol. Oncol 12, 18 (2019). [PubMed: 30777106]
44. Jana S et al. Transcriptional–translational conflict is a barrier to cellular transformation and cancer progression. Cancer Cell 41, 853–870.e13 (2023). [PubMed: 37084735]
45. Sfakianos AP, Raven RM & Willis AE The pleiotropic roles of eIF5A in cellular life and its therapeutic potential in cancer. Biochem. Soc. Trans 50, 1885–1895 (2022). [PubMed: 36511302]
46. Clarke SG Protein methylation at the surface and buried deep: thinking outside the histone box. Trends Biochem. Sci 38, 243–252 (2013). [PubMed: 23490039]
47. Mealey-Farr R et al. Antibody toolkit to investigate eEF1A methylation dynamics in mRNA translation elongation. J. Biol. Chem 299, 104747 (2023). [PubMed: 37094697]
48. Simsek D & Barna M An emerging role for the ribosome as a nexus for post-translational modifications. Curr. Opin. Cell Biol 45, 92–101 (2017). [PubMed: 28445788]
49. Tian X, Ju H & Yang W An ego network analysis approach identified important biomarkers with an association to progression and metastasis of gastric cancer. J. Cell. Biochem 120, 15963–15970 (2019). [PubMed: 31081222]
50. Reynoird N et al. Coordination of stress signals by the lysine methyltransferase SMYD2 promotes pancreatic cancer. Genes Dev 30, 772–785 (2016). [PubMed: 26988419]
51. Van Aller GS et al. Smyd3 regulates cancer cell phenotypes and catalyzes histone H4 lysine 5 methylation. Epigenetics 7, 340–343 (2012). [PubMed: 22419068]
52. Edmunds JW, Mahadevan LC & Clayton AL Dynamic histone H3 methylation during gene induction: HYPB/Setd2 mediates all H3K36 trimethylation. EMBO J 27, 406–420 (2008). [PubMed: 18157086]
53. Schotta G et al. A chromatin-wide transition to H4K20 monomethylation impairs genome integrity and programmed DNA rearrangements in the mouse. Genes Dev 22, 2048–2061 (2008). [PubMed: 18676810]
54. Pagans S et al. The cellular lysine methyltransferase Set7/9-KMT7 binds HIV-1 TAR RNA, monomethylates the viral transactivator Tat, and enhances HIV transcription. Cell Host Microbe 7, 234–244 (2010). [PubMed: 20227666]
55. Luger K, Rechsteiner TJ & Richmond TJ in Chromatin Protocols. Methods in Molecular Biology, vol. 119 (ed. Becker PB) 1–16 (1999).
56. Zoabi M et al. Methyltransferase-like 21 C (METTL21C) methylates alanine tRNA synthetase at Lys-943 in muscle tissue. J. Biol. Chem 295, 11822–11832 (2020). [PubMed: 32611769]
57. Baymaz HI, Spruijt CG & Vermeulen M in Stable Isotope Labeling by Amino Acids in Cell Culture (SILAC). Methods Mol. Biol, vol. 1188 (ed. Warscheid B) 207–226 (2014).
58. Wingfield P Protein precipitation using ammonium sulfate. Curr. Protoc. Protein. Sci Appendix 3:Appendix-3F (2001).

59. Cox J & Mann M MaxQuant enables high peptide identification rates, individualized p.p.b.-range mass accuracies and proteome-wide protein quantification. Nat. Biotechnol 26, 1367–1372 (2008). [PubMed: 19029910]
60. Bushnell B BBMap: A Fast, Accurate, Splice-Aware Aligner (Lawrence Berkeley National Lab, 2014).
61. Quast C et al. The SILVA ribosomal RNA gene database project: improved data processing and web-based tools. Nucleic Acids Res 41, D590–D596 (2013). [PubMed: 23193283]
62. Kim D, Langmead B & Salzberg SL HISAT: a fast spliced aligner with low memory requirements. Nat. Methods 12, 357–360 (2015). [PubMed: 25751142]
63. Liao Y, Smyth GK & Shi W The R package Rsubread is easier, faster, cheaper and better for alignment and quantification of RNA sequencing reads. Nucleic Acids Res 47, e47 (2019). [PubMed: 30783653]
64. Pruitt KD et al. RefSeq: an update on mammalian reference sequences. Nucleic Acids Res 42, D756–D763 (2013). [PubMed: 24259432]
65. Robinson MD, McCarthy DJ & Smyth GK edgeR: a Bioconductor package for differential expression analysis of digital gene expression data. Bioinformatics 26, 139–140 (2009). [PubMed: 19910308]
66. Ritchie ME et al. limma powers differential expression analyses for RNA-sequencing and microarray studies. Nucleic Acids Res 43, e47 (2015). [PubMed: 25605792]
67. Stacklies W, Redestig H, Scholz M, Walther D & Selbig J pcaMethods—a Bioconductor package providing PCA methods for incomplete data. Bioinformatics 23, 1164–1167 (2007). [PubMed: 17344241]
68. Wang L, Wang S & Li W RSeQC: quality control of RNA-seq experiments. Bioinformatics 28, 2184–2185 (2012). [PubMed: 22743226]
69. Subramanian A et al. Gene set enrichment analysis: a knowledge-based approach for interpreting genome-wide expression profiles. Proc. Natl Acad. Sci. USA 102, 15545–15550 (2005). [PubMed: 16199517]
70. Mootha VK et al. PGC-α-responsive genes involved in oxidative phosphorylation are coordinately downregulated in human diabetes. Nat. Genet 34, 267–273 (2003). [PubMed: 12808457]
71. Korotkevich G et al. Fast gene set enrichment analysis. Preprint at bioRxiv 10.1101/060012 (2021).
72. Guan B-J et al. A unique ISR program determines cellular responses to chronic stress. Mol. Cell 68, 885–900.e6 (2017). [PubMed: 29220654]
73. Mansour FH & Pestov DG Separation of long RNA by agarose–formaldehyde gel electrophoresis. Anal. Biochem 441, 18–20 (2013). [PubMed: 23800830]
74. Rahman S & Zenklusen D in Imaging Gene Expresson. Methods in Molecular Biology, vol. 1042 (ed. Shav-Tal Y) 33–46 (Humana Press, 2013).
75. Scott DD et al. Nol12 is a multifunctional RNA binding protein at the nexus of RNA and DNA metabolism. Nucleic Acids Res 45, 12509–12528 (2017). [PubMed: 29069457]
76. Evans R et al. Protein complex prediction with AlphaFold-Multimer. Preprint at bioRxiv 10.1101/2021.10.04.463034 (2022).
77. The Cancer Genome Atlas Research Network. Comprehensive molecular characterization of gastric adenocarcinoma. Nature 513, 202–209 (2014). [PubMed: 25079317]
78. Gao J et al. Integrative analysis of complex cancer genomics and clinical profiles using the cBioPortal. Sci. Signal. 6, pl1 (2013). [PubMed: 23550210]
79. Cerami E et al. The cBio cancer genomics portal: an open platform for exploring multidimensional cancer genomics data. Cancer Discov 2, 401–404 (2012). [PubMed: 22588877]
80. Mazur PK et al. SMYD3 links lysine methylation of MAP3K2 to Ras-driven cancer. Nature 510, 283–287 (2014). [PubMed: 24847881]
81. Boussadia O, Kutsch S, Hierholzer A, Delmas V & Kemler R E-cadherin is a survival factor for the lactating mouse mammary gland. Mech. Dev 115, 53–62 (2002). [PubMed: 12049767]
82. Jonkers J et al. Synergistic tumor suppressor activity of BRCA2 and p53 in a conditional mouse model for breast cancer. Nat. Genet 29, 418–425 (2001). [PubMed: 11694875]

83. Lesche R et al. Cre/loxP-mediated inactivation of the murine Pten tumor suppressor gene. Genesis 32, 148–149 (2002). [PubMed: 11857804]

84. Gao X et al. ES cell pluripotency and germ-layer formation require the SWI/SNF chromatin remodeling component BAF250a. Proc. Natl Acad. Sci. USA 105, 6656–6661 (2008). [PubMed: 18448678]

85. Hingorani SR et al. Preinvasive and invasive ductal pancreatic cancer and its early detection in the mouse. Cancer Cell 4, 437–450 (2003). [PubMed: 14706336]

86. Skarnes WC et al. A conditional knockout resource for the genome-wide study of mouse gene function. Nature 474, 337–342 (2011). [PubMed: 21677750]

87. Raymond CS & Soriano P High-efficiency FLP and PhiC31 site-specific recombination in mammalian cells. PLoS ONE 2, e162 (2007). [PubMed: 17225864]

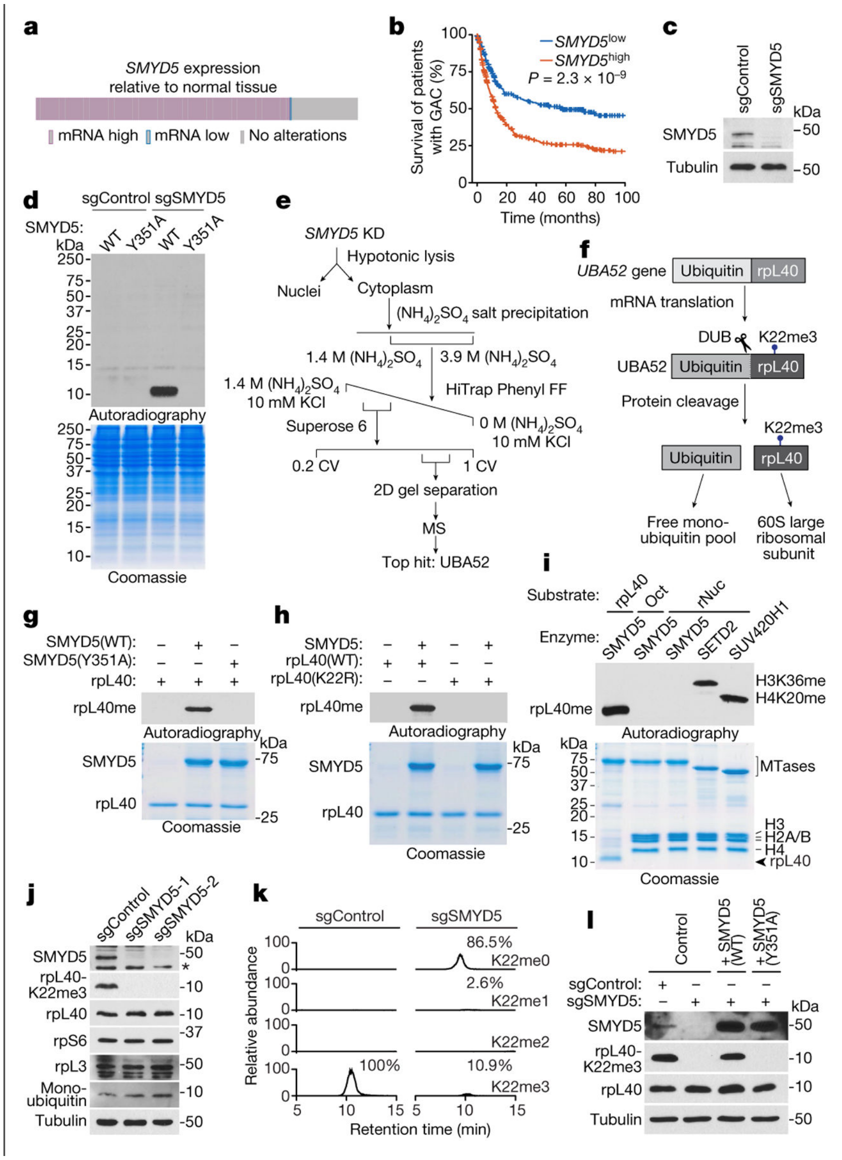

Fig. 1 |. The principal physiological activity of SMYD5 is rpL40K22 methylation.

a, *SMYD5* overexpression in GAC versus normal stomach tissue (data from The Cancer Genome Atlas (TCGA); *n* = 412 patients). **b**, *SMYD5* expression negatively correlates with survival for patients with GAC (*n* = 640). *P* values determined by log-rank test. **c**, Western blots with indicated antibodies of whole cell extracts (WCEs) from A549 cells treated with sgRNA against *SMYD5* (sgSMYD5) or control sgRNA (sgControl). **d**, SMYD5 methylates an approximate 10 kDa protein in WCEs. In vitro methylation assays with recombinant wild-type SMYD5 (SMYD5(WT)) or catalytically dead SMYD5 (SMYD5(Y351A)) using indicated WCEs shown in **c** as the substrate. Top, ^{3}H-SAM was used as the methyl donor and methylation was visualized by autoradiography. Bottom, Coomassie stain of proteins present in reactions. **e**, Schematic to enrich the SMYD5-dependent methylated band, with the top hit UBA52 indicated. CV column volumes; KD, knockdown; MS, mass spectrometry. **f**, *UBA52* encodes a precursor protein that is cleaved by deubiquitinase (DUB) into monoubiquitin and rpL40, a 60S large subunit component trimethylated at K22. **g**,**h**, SMYD5 specifically methylates rpL40K22. In vitro methylation assays as in **d** using indicated enzymes and substrates. **i**, SMYD5 methylates rpL40, but not histones. In vitro methylation assays as in **d** with indicated enzyme and substrates. Oct, histone octamer; rNuc, recombinant nucleosome. SETD2 and SUV420H1 are positive controls for the methylation of H3K36 and H4K20, respectively. **j**, Western blots with the indicated antibodies of SMYD5-depleted KKLS WCEs using two independent *SMYD5* sgRNAs. Asterisk indicates a nonspecific band. Tubulin was used as the loading control. **k**, Trimethylation is the predominant methylation state at rpL40K22 in KKLS cells and is depleted after *SMYD5* knockdown. Selected ion chromatograms for non-, mono-, di- and tri-methyl rpL40K22 peptides are shown. HPLC elution profiles show a 10-ppm mass window around expected peptide masses (peptide sequence ICR$\underline{\text{K}}$CY, K22 is underlined; *m/z*: 300.4791 (me0), 305.1509 (me1), 309.8228(me2) and 314.4947 (me3)). **l**, Western blots of SMYD5-depleted KKLS cells complemented with CRISPR-resistant SMYD5(WT), SMYD5(Y351A) or control plasmid.

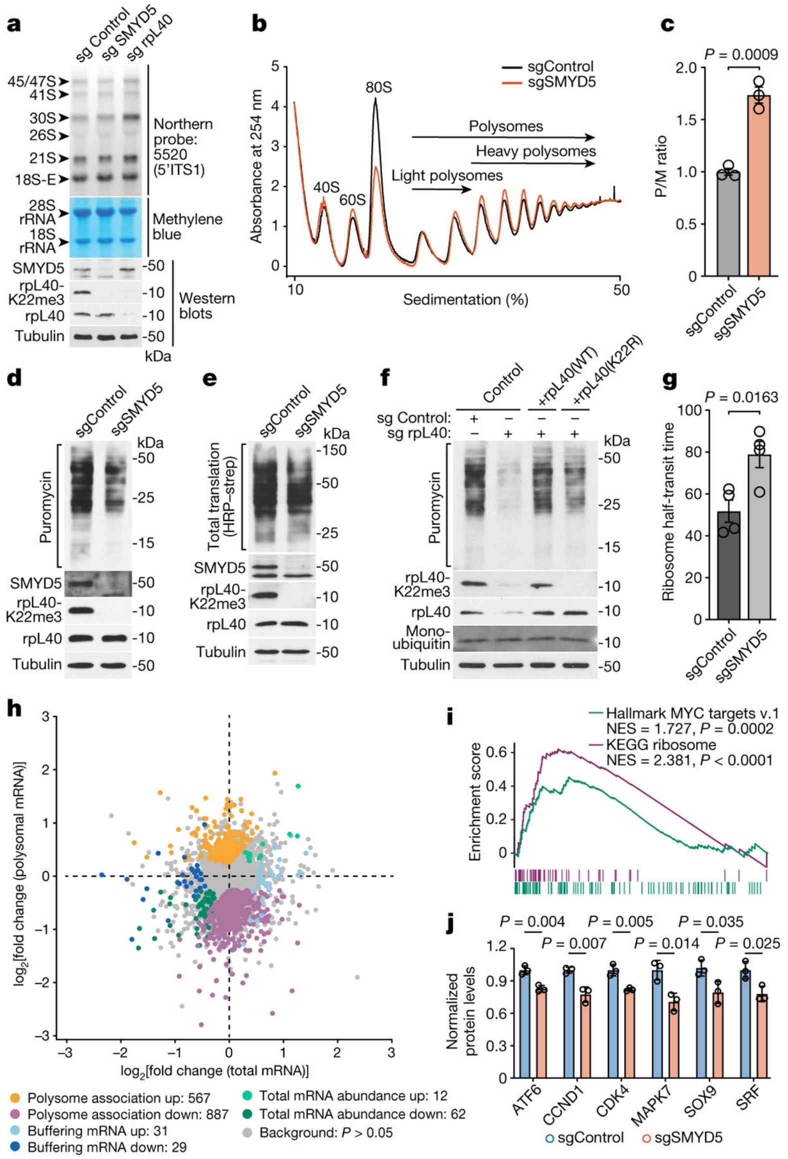

Fig. 2 |. SMYD5 methylation of rpL40K22 regulates elongation rates and protein synthesis.

a, rpL40K22me3 loss does not affect ribosome biogenesis. Indicated pre-rRNA (top: northern blot) and mature rRNAs (middle: methylene blue) levels from indicated cell lines. Bottom, western blot of WCEs as indicated. Northern blot probe (5520) targets the 5′-ITS1 pre-rRNA region. **b**, Polysome profiles of KKLS cell extracts with or without SMYD5 depletion. 40S and 60S ribosomal subunits, 80S monosome and light (≤3 ribosomes) and heavy (>3 ribosomes) polysome distribution is indicated (western blots in Extended Data Fig. 6a). **c**, P/M ratio as in **b**. **d**,**e**, SMYD5 depletion reduces global protein synthesis. **d**, Puromycylation assays in KKLS cells with or without SMYD5 depletion. WCEs were probed with the indicated antibodies. **e**, AHA labelling assays as in **d**. HRP–streptavidin (HRP–strep) detects biotin-clicked AHA. **f**, rpL40(K22R) substitution reduces global protein synthesis. Puromycylation assays and western blots of WCEs in control or rpL40-depleted LMSU cells complemented with CRISPR-resistant rpL40(WT), rpL40(K22R) or control plasmids. **g**, SMYD5 depletion decreases mRNA translation elongation rates. Ribosome half-transit time in the indicated cell lines. **h**, rpL40K22me3 regulation of polysome-associated mRNAs. Polysome association, mRNAs differentially associated (up/down) with polysomes without total mRNA abundance changes. Buffering mRNA, total mRNA up/down without corresponding changes in polysome association. Total mRNA abundance, total mRNA increased/decreases with congruent changes in polysome association. Background, mRNAs with no significant change. **i**, GSEA identifies enrichment of MYC targets and ribosome gene signatures in differential polysome-associated mRNAs from control versus SMYD5-depleted KKLS cells ($n = 3$ biologically independent samples per group). Normalized enrichment scores (NES) and nominal P values are provided (Methods). **j**, Quantification of indicated protein levels in KKLS cells with or without SMYD5 depletion. See Extended Data Fig. 6k,l for representative western blots and mRNA levels. P values determined by two-tailed unpaired t-test (**c**,**g**,**j**). Data are the means ± s.e.m. of three (**c**,**j**) or four (**g**) independent biological replicates.

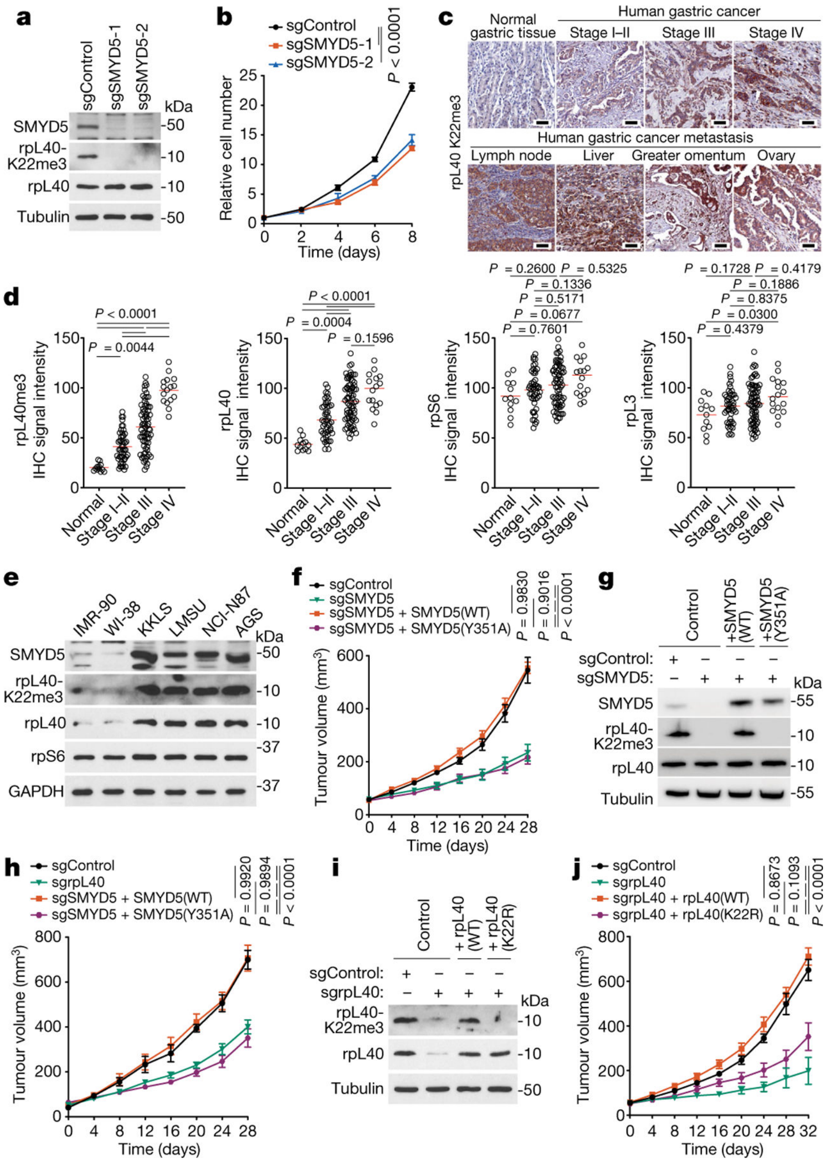

Fig. 3 |. The SMYD5–rpL40me3 axis is upregulated in gastric cancer and promotes GAC cell xenograft and PDX tumour growth in vivo.

a,**b**, SMYD5 depletion inhibits LMSU cell proliferation. **a**, Western blots with indicated antibodies of WCEs with or without SMYD5 depletion. **b**, Proliferation rates of cells in **a** from three biologically independent experiments. **c**, Representative rpL40K22me3 IHC staining of patient samples from normal gastric tissue ($n = 12$), GAC at advancing stages (I–II, $n = 48$; III, $n = 72$; IV, $n = 16$) and metastasis at indicated organs ($n = 34$). Scale bars, 100 μm. **d**, Quantification of IHC chromogen stain intensity for rpL40K22me3, rpL40, rpS6 and rpL3 as indicated in normal gastric tissue ($n = 12$) and advancing stages of GAC (I–II, $n = 48$; III, $n = 72$; IV, $n = 16$). Red line indicates median. **e**, Western blot analyses showing that SMYD5, rpL40K22me3 and total rpL40 levels are higher in four different GAC cell lines than in non-transformed IMR-90 and WI-38 cell lines. **f**, SMYD5 catalytic activity is required for full LMSU xenograft tumour growth. Tumour volume quantification for LMSU xenografts was modified to deplete endogenous SMYD5 (sgSMYD5) and overexpressing CRISPR-resistant SMYD5(WT) or SMYD5(Y351A) (see Extended Data Fig. 4g for western blot analyses) in NSG mice ($n = 6$ mice per group). **g**, Western blot analysis with the indicated antibodies of GAC PDX $CDH^{1A617T}TP53^{X307\_splice}$ WCEs modified ex vivo to express sgSMYD5 or sgControl and overexpressing CRISPR-resistant SMYD5(WT) or SMYD5(Y351A) as indicated. **h**, Tumour volume quantification for GAC PDX $CDH^{1A617T}TP53^{X307\_splice}$ xenografts as in **g** in NSG mice ($n = 6$ mice per group). **i**, Western blot analysis with the indicated antibodies of WCEs of rpL40-depleted LMSU cells complemented with CRISPR-resistant rpL40(WT) or rpL40(K22R). **j**, Tumour volume quantification for LMSU xenografts as in **i** in NSG mice ($n = 6$ mice per group). P values determined by two-way analysis of variance (ANOVA) with Tukey's post hoc test (**d**,**f**,**h**,**j**) or two-tailed unpaired t-test (**b**). Data are represented as the mean ± s.e.m. (**b**,**f**,**h**,**j**).

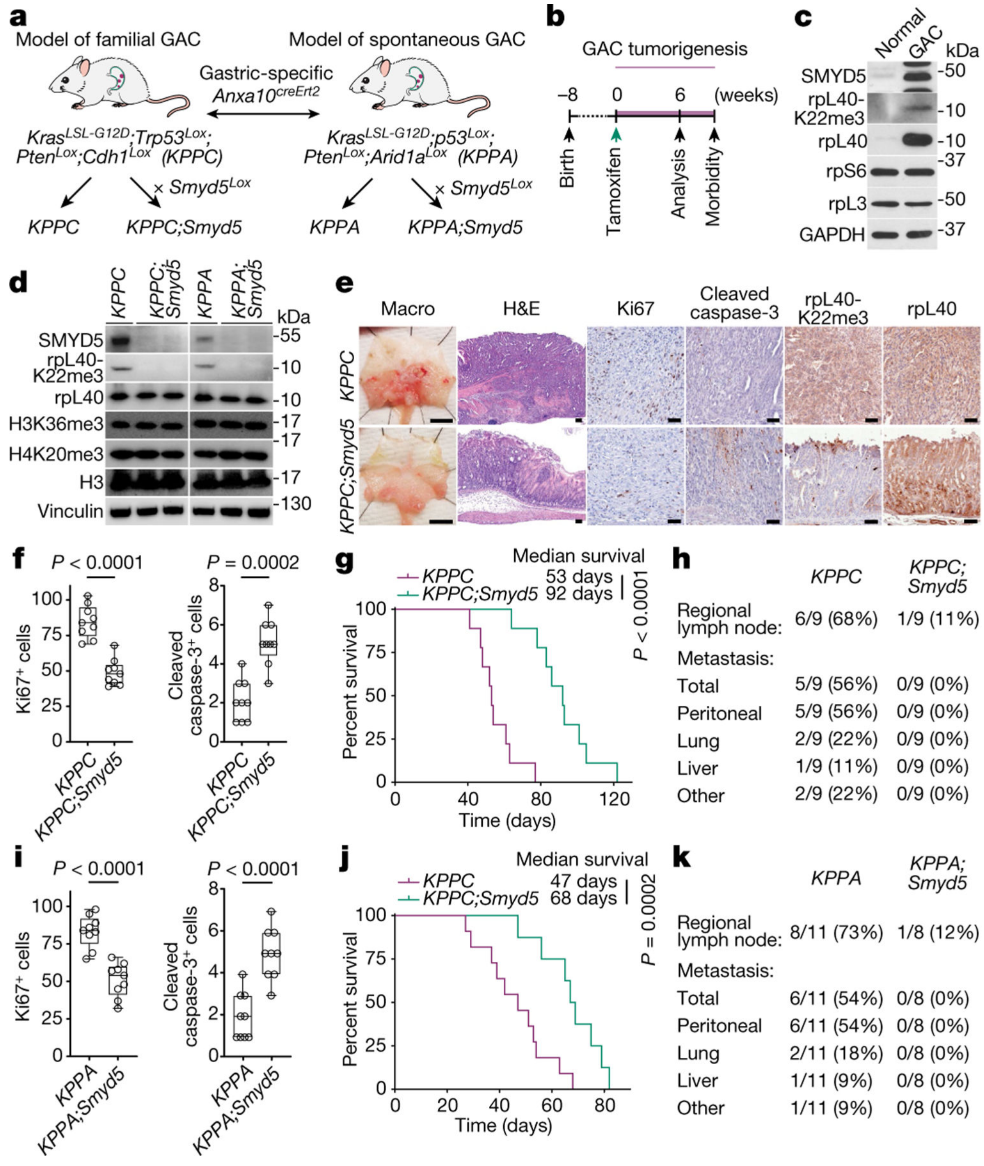

h

	KPPC	*KPPC; Smyd5*
Regional lymph node:	6/9 (68%)	1/9 (11%)
Metastasis:		
Total	5/9 (56%)	0/9 (0%)
Peritoneal	5/9 (56%)	0/9 (0%)
Lung	2/9 (22%)	0/9 (0%)
Liver	1/9 (11%)	0/9 (0%)
Other	2/9 (22%)	0/9 (0%)

k

	KPPA	*KPPA; Smyd5*
Regional lymph node:	8/11 (73%)	1/8 (12%)
Metastasis:		
Total	6/11 (54%)	0/8 (0%)
Peritoneal	6/11 (54%)	0/8 (0%)
Lung	2/11 (18%)	0/8 (0%)
Liver	1/11 (9%)	0/8 (0%)
Other	1/11 (9%)	0/8 (0%)

Fig. 4 |. SMYD5 ablation inhibits malignant gastric cancer progression in vivo.

a, Schematic of generation of familial (*KPPC*) and spontaneous (*KPPA*) mouse models of GAC with *Smyd5* deletion. Tamoxifen-induced recombination of mutant alleles is mediated using a gastric-specific *Anxa10*^{creErt2} strain. **b**, Experimental design to assess effects of SMYD5 ablation on GAC pathogenesis in *KPPC* and *KPPA* models. **c**, Western blot analysis with indicated antibodies of representative lysates of tissue biopsies from normal stomach and GAC from *KPPC* mice. **d**, Western blot analysis with indicated antibodies of representative lysates of tumour biopsies from indicated mouse models at 6 weeks after tamoxifen induction. Vinculin and total H3 are shown as loading controls. **e**, Representative macro pathology, H&E and IHC staining with indicated antibodies of gastric tumours from *KPPC* and *KPPC;Smyd5* mutant mice at 6 weeks after tamoxifen induction ($n = 9$ per group). Scale bars, 5 mm (whole mount) and 100 μm (histology). **f**, Quantification of proliferation (Ki67$^+$), cell death (cleaved caspase-3$^+$) in *KPPC* and *KPPC;Smyd5* samples as in **e**. **g**, Kaplan–Meier survival curves of *KPPC* control mice (*n* = 9) and *KPPC;Smyd5* mutant mice (*n* = 9). **h**, Clinical spectrum of malignant gastric cancer in *KPPC* models with or without SMYD5 ablation, including observed frequency of regional lymph nodes and distant organ metastases. **i**, Quantification of proliferation and cell death as in **f** in *KPPA* and *KPPA;Smyd5* samples (*n* = 9 per group) (Extended Data Fig. 8h). **j**, Kaplan–Meier survival curves of *KPPA* control mice (*n* = 11) and *KPPC;Smyd5* mutant mice (*n* = 8). **k**, Clinical spectrum of malignant gastric cancer in *KPPA* model with or without SMYD5 ablation, including observed frequency of regional lymph nodes and distant organs metastases. *P* values determined by two-tailed unpaired *t*-test (**f**,**i**) or log-rank test (**g**,**j**). Boxes indicate 25th to 75th percentiles, whiskers the minimum to maximum values, and the centre line the median.

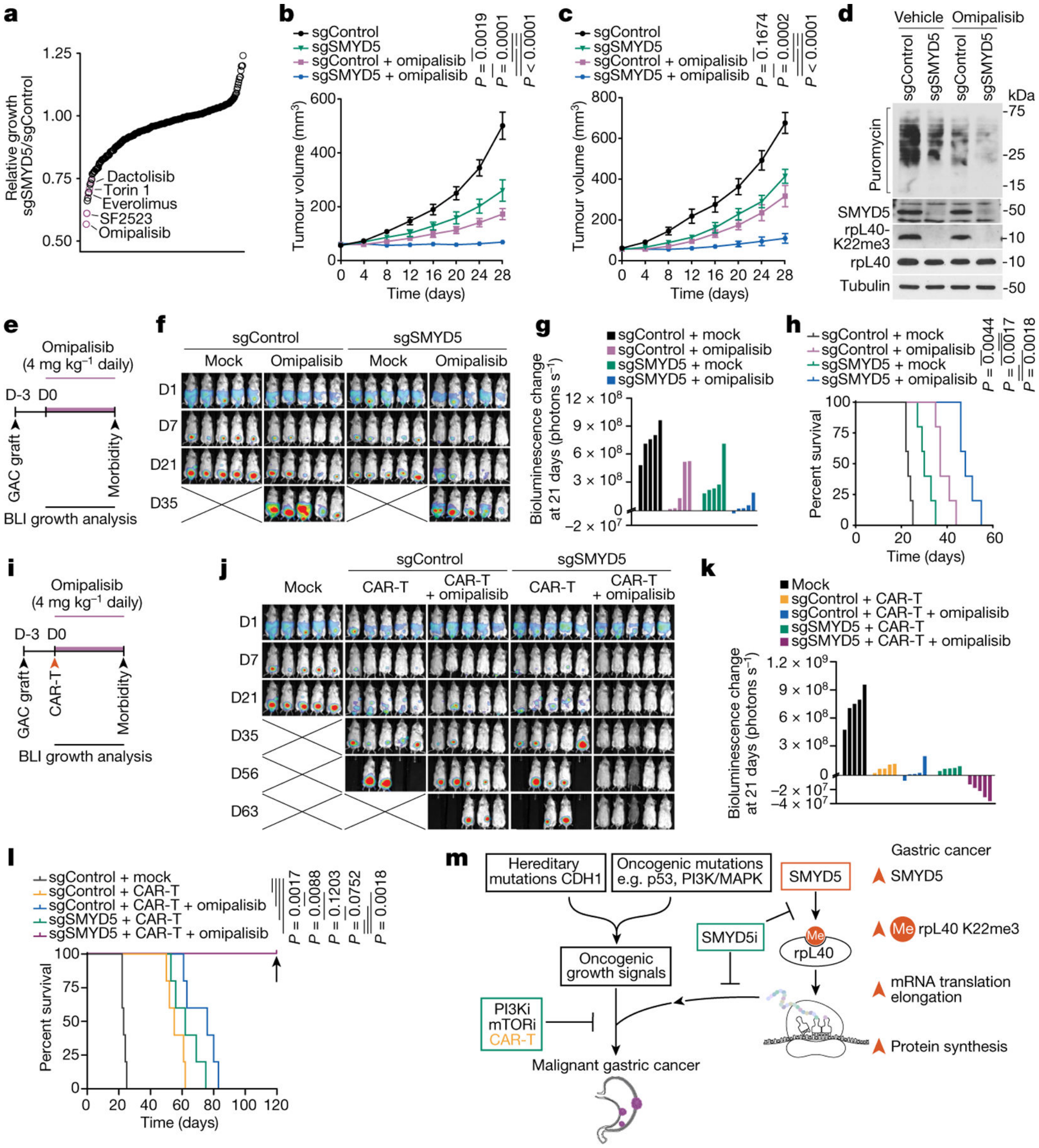

Fig. 5 |. SMYD5 depletion cooperates with PI3K–mTOR inhibitors and CAR-T therapeutics to treat malignant GAC.

a, Comparative drug screen identifies potential synergy between PI3K–mTOR inhibitors and SMYD5 depletion (Supplementary Table 5). Several top hits are indicated. **b**,**c**, Quantification of tumour growth in LMSU xenograft (**b**) and $CDH1^{A617T}TP53^{X307\_splice}$ GAC PDX (**c**) with or without SMYD5 depletion in NSG mice treated with omipalisib (4 mg kg^{-1} daily, n = 5 mice per group) or vehicle control. **d**, Puromycylation assays in LMSU cells with or without SMYD5 depletion treated with either vehicle or omipalisib (50 nM) for 16 h. WCEs were probed with the indicated antibodies. **e**, Schematic of PC mouse model experimental design. BLI, bioluminescence imaging; D, day. **f**, Representative BLI of PC mice receiving indicated treatment (n = 5 mice per group). Scales normalized for all time points. **g**, Waterfall plot of NUGC4 PC xenograft BLI signal changes at day 21 in individual mice receiving the indicated therapy. **h**, Kaplan–Meier survival curves of mice with NUGC4 PC xenografts receiving the indicated treatment. **i**, Experimental design to assess MSLN–CAR-T-cell-based combination therapies in the PC mouse model. **j**, Representative BLI of PC mice receiving the indicated treatment as in **f**. **k**, Waterfall plot as in **g** with the indicated treatments. **l**, Triple therapy results in long-term tumour-free survival in the PC model system. Kaplan–Meier survival curves as in **h** in mice receiving the indicated treatments. Arrow indicates the time the study was completed. sgControl + mock cohort data in **j**–**l** is the same as in **f**–**h**. **m**, Model for the role of SMYD5 in GAC pathogenesis. SMYD5, rpL40 and rpL40K22me3 upregulation in GAC increases oncogenic gene expression programs at the level of protein synthesis, potentially through enhanced elongation. These activities converge with divergent GAC drivers and oncogenic growth signals to promote GAC evolution into malignant disease. SMYD5 inhibition (SYMD5i) may cooperate with targeted (inhibition of PI3K (PI3Ki) and mTOR (mTORi)) and cell-based therapies (CAR-T) to mitigate GAC progression. *P* values determined by two-way ANOVA with Tukey's post hoc test (**b**,**c**) or log-rank test (**h**,**l**). Data represented as the mean ± s.e.m. (**b**,**c**).